

Quantum Simulators with Trapped Ions: Two Examples

Georgetown University

Thomas Kiely

May 2018

Abstract

Ultracold ion traps are powerful tools for probing the dynamics of quantum many body systems and may potentially be the basis for future quantum computing technology. Rather than numerically solving the Schrodinger equation to determine the evolution of large quantum mechanical systems, which can be arduous if not impossible, ultracold ion traps can simulate the evolution of quantum many-body Hamiltonians so that they do not need to be solved. In order for this technology to be reliably applied, however, the classical and quantum dynamics of ions within the trap must be understood by comparing experimental results to computational simulation for small ($n \leq 10$) systems. We present two analyses of phenomena in small quantum many-body systems: first, we clarify the relationship between the transverse-field Ising model and the XY model for a linear chain of trapped ions; then, we analyze the dynamics of a structural transition between two conformations of a two-dimensional Coulomb crystal. In each case, we hope our results contribute to a more robust understanding of quantum many-body physics that can be applied to both to ultracold trapped ion simulation and to a broad spectrum of related phenomena.

Contents

1	Introduction	4
1.1	Overview	4
1.2	Motivation	6
1.2.1	Quantum Computing	6
1.2.2	Structural Transition	8
2	Relationship between the transverse-field Ising model and the XY model via the rotating-wave approximation	10
2.1	Introduction	11
2.2	Formalism	13
2.2.1	Spin Exchange Coefficients	13
2.2.2	Time Evolution	14
2.2.3	Energy Levels	14
2.2.4	Wavefunction Overlap	17
2.2.5	Green's Function	20
2.3	Results	22
2.4	Conclusions	25
3	Conformational Transition in Trapped-Ion Coulomb Crystal	26
3.1	Computational Simulation	27
3.1.1	Derivation of the Oblate Paul Trap Potential	27
3.1.2	Transition State Theory	31
3.1.3	Minimum Energy Path (MEP)	32
3.1.4	Results	40
3.2	Data Analysis	44
3.2.1	Markov Chain	44
3.2.2	Continuous Time Markov Chain	45
3.2.3	Results	46

3.3	Conclusions	50
4	Final Remarks	51
4.1	Rough Timeline	51
4.2	Acknowledgments	52

Chapter 1

Introduction

1.1 Overview

In 1964, Richard Feynman, largely considered the most prominent physicist of the second half of the twentieth century, famously claimed that “nobody understands quantum mechanics” [1]. While advancements have been made since then, quantum many body systems are still far too complex to model using conventional computers. The reason for this is that the dimensions of quantum many body systems grow exponentially in Hilbert space as the number of particles increases, while those of classical many body systems grow linearly. A solution to this problem, also proposed by Feynman, is quantum simulation: to allow a quantum system to evolve on its own, and to observe the resulting time-evolved states [2]. A quantum simulator that can simulate *any* quantum state is a universal quantum simulator, or a quantum computer.

Some of the best current realization of quantum simulators use ultracold trapped ions. In these simulators, ions are spatially confined within the trap and cooled until they form a regular array known as a Coulomb crystal. The Coulomb crystal is used to simulate a lattice spin structure, where each trapped ion corresponds to a particle with a spin. The quantum “spin state” is encoded into two of the hyperfine energy states of each ion. By illuminating all the ions with laser radiation, spin-spin and magnetic field interactions can be simulated via coupling to the phonon modes of the crystal [3]. This allows for the creation of particular many-body Hamiltonians that can be evolved in time, after which the internal energy states of the ions may be measured

to give a final state of the system.

In this thesis, we present two projects based on ultracold trapped ions. The first is investigation into the relationship between the transverse-field Ising model and the XY model in a one-dimensional three-layer Paul trap. These are two different many-body Hamiltonians that can be simulated by ultracold trapped ions, although the former is much easier to simulate in a Paul trap than the latter. The relationship between these models has previously been understood in terms of the rotating-wave approximation, which leads to a stroboscopic mapping of the TF Ising model onto the XY model. We compute the time-evolution of small Hamiltonians (up to eleven ions) in order to determine constraints for experimentalists making use of this mapping, and we use a perturbative treatment of the transverse-field Ising model Hamiltonian to explain the mapping more concretely.

The second project is an analysis of the dynamics of a structural transition between two states of a six-ion Coulomb crystal in a two-dimensional oblate Paul trap. The ions sit in a two-dimensional anharmonic oscillator potential and repel each other via the Coulomb force. The two orientations in question are an open ring, in which all six ions form a ring, and a closed ring, in which of the five ions form a ring and one ion sits in the center. This transition has been observed experimentally by Dr. Wes Campbell and his group at UCLA, with whom we have been collaborating. Using computational modelling and transition state theory, we have been able to characterize the energy barrier between these states and estimate both classical and quantum rates of transition. Using data taken by the Campbell group, we would like to use our models to determine properties of the experimental transition such as the actual transition pathway and the effective temperature of the ions. We are still awaiting the data from the Campbell group necessary to perform these calculations, however, so I can only present a sketch of how these calculations would be performed.

Both of these projects concern the dynamics of quantum many-body systems that can be created and controlled in ultracold trapped ion simulators. The general scope of our work is to improve the understanding of the classical and quantum mechanical phenomena that occurs in these simulators and to provide test cases against which simulator results can be compared. To this latter point, it is impossible to test large-scale quantum simulators against numerically-generated results for reasons that I will expand upon in the next section. Rather, the results from these simulators must be compared to numerical results for small systems to determine their experimental

limitations. Quantum chemistry calculations, of the sort that are related to our second project, have historically been used as some of the first test cases for quantum computers. The results that we present here are part of a body of work that is used to test the efficacy of current quantum simulators, and which may eventually be used to test the efficacy of trapped ion quantum computers.

1.2 Motivation

1.2.1 Quantum Computing

To motivate these inquiries, I will present some background information on the nature of quantum computing, which is the most well-known potential application of ultracold ion trap technology. This section will begin with an introduction to classical computers before addressing quantum computers.

Classical computers operate by using electric circuits to evaluate logic statements. Logic statements are composed of logic gates, which apply standard Boolean (true or false) operations. Common examples of logic gates are the AND gate and the OR gate. In each case, the input(s) are binary bits: either 0 or 1, or in the case of a circuit, “on” or “off”. An AND gate will take two binary input signals and output “on” if both signals are “on”, and “off” in all other cases. An OR gate inputs two binary signals as well, but its output is “off” if both signals are “off”, and “on” in all other cases.

Complex operations in classical computers are built out of a series of binary logic gates, and all data used in these operations must be translated into bits at some point in time. Computer scientists use these structural limitations to determine the time complexity of algorithms, which approximates the time an algorithm takes to run as a function of the size of the system. Quantum many body systems fall under the category of “exponential time”, which is to say that the running time scales as the exponential of the size of the system. Consider, for example, a system of n particles wherein each particle has two distinct states ($|\uparrow\rangle$ or $|\downarrow\rangle$). If the system is classical, the state of the system can be classified at any given time by specifying whether each particle is in the $|\uparrow\rangle$ state or the $|\downarrow\rangle$ state, which is a $1 \times n$ vector. If this is a quantum mechanical system, though, each possible superposition of states (e.g. $|\uparrow\uparrow\uparrow\dots\rangle$, $|\uparrow\uparrow\downarrow\dots\rangle$, etc.) may have a non-zero probability amplitude, so the state of the system must be classified with a 1×2^n vector.

It is for this reason that, while a quantum mechanical system of 5 or 10 particles can be simulated on classical computers, simulating systems of 200 particles or more is virtually unthinkable (assuming each particle has only two states, the state vector would have $2^{200} \approx 10^{60}$ components).

Richard Feynman proposed the idea of a universal quantum simulator, or a quantum computer, that could simulate any quantum system [2]. In such a device, the bits of a conventional computer would be replaced by “qubits”, or quantum bits. These are two-state quantum systems, which means their state vector is a quantum superposition of $| \uparrow \rangle$ and $| \downarrow \rangle$. This means that 2^n variables can be encoded into the state of an n -qubit system (for the reasons stated above). Furthermore, the set of operations that a quantum computer could apply is larger than that of a standard computer. If we think of logic gates as matrices that act on a state vector, the class of logic gates that a classical computer can apply is encompassed by stochastic matrices, which preserve the sum of the probabilities of each state. While operations given by stochastic matrices may be used as quantum logic gates, operations given by unitary matrices, or matrices that conserve the sum of the squared probability amplitudes, may be used as well. This flexibility allows for the creation of quantum algorithms to solve problems that are unreasonable to solve in classical computation. Shor’s algorithm and Grover’s algorithm, for example, drastically improve upon the best classical algorithms for factoring large numbers and for searching through unordered lists, respectively.

While we may already know what quantum algorithms we would use on a quantum computer, the hardware has yet to be realized. Qubits must be physical, quantum mechanical systems that are isolated from thermal fluctuations and have long decoherence times, and whose interactions can be finely tuned and quickly adjusted. It is an active field of research to determine which quantum systems would best satisfy these criteria.

Ultracold trapped ion simulators are among the top candidates for future quantum computing technology. They are presently used as “analog” quantum computers, in that they can solve quantum many body problems for specific Hamiltonians. While analog quantum computers lack the flexibility necessary for quantum computation, the results of trapped ion experiments will be crucial for future advancements in quantum computer hardware.

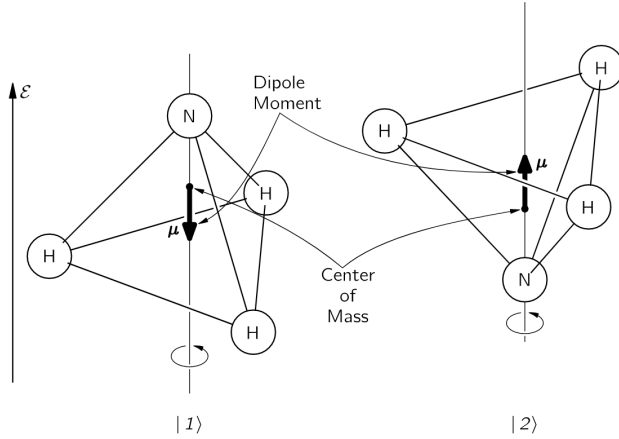


Figure 1.1: A diagram of nitrogen inversion: the dipole moment is antiparallel to the angular velocity in $|1\rangle$ and parallel in $|2\rangle$. This image is taken from [5]

1.2.2 Structural Transition

Structural transitions are phase transitions within a crystal from one structural orientation to another. Strictly speaking, it only makes sense to speak of structural transitions when dealing with large, statistical systems. In our second project, we are investigating the reconfiguration of a six-ion Coulomb crystal. This might be more closely related to conformational changes in large molecules than to structural transitions in statistical mechanics, but we have chosen to retain the terminology to clarify that this is a crystal transition.

A potential analog to this transition is Nitrogen inversion, which occurs in the Ammonia molecule. Ammonia consists of three Hydrogen atoms and one Nitrogen atom in a trigonal pyramidal geometry. When rotating about an axis that is perpendicular to the plane of Hydrogen atoms and that intersects the Nitrogen atom, the molecule can be in one of two states: that in which the dipole moment is parallel to angular velocity of the molecule, and that in which it is antiparallel [5]. In essence, the transition between these two states amounts to the Nitrogen atom moving from above the plane of Hydrogen atoms to below it, or vice versa, as is shown in figure 1.1. The necessity for rotation about the axis of symmetry serves only to exclude that these two states exhibit mirror symmetry.

Classically, however, the Nitrogen atom ought to be confined to one side

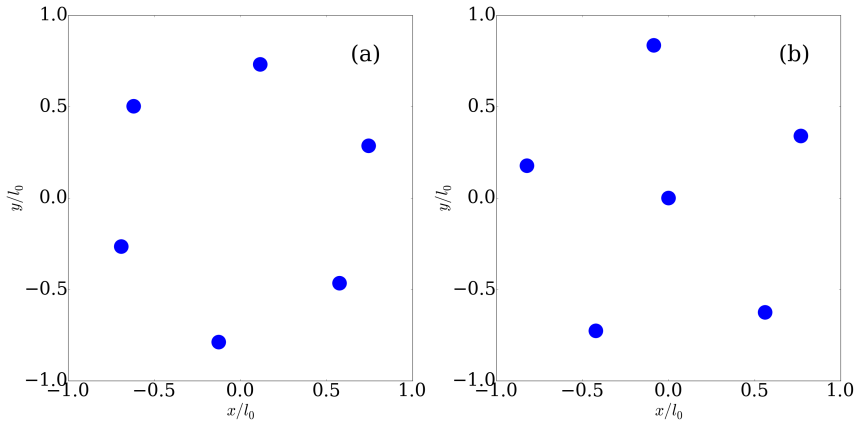


Figure 1.2: The two conformations of the Coulomb crystal. The open configuration is shown in (a), and the closed configuration is shown in (b).

of the plane of Hydrogen atoms. Classical transitions across potential boundaries depend on thermal fluctuations, which have an energy scale on the order of $k_B T$. By varying the temperature and measuring the probability of transitioning, experimentalists can determine if a transition is classical in nature. If the transition probability is temperature-invariant, then we would have good reason to believe it to be an instance of quantum tunneling (or, in some cases, an alternative form transition that is not thermally activated). This is the case with Nitrogen inversion: the Nitrogen atom tunnels across the sharp potential boundary created by the plane of Hydrogen atoms.

We are analyzing a structural transition in a two-dimensional Coulomb crystal, which is made up of six ions confined to a plane by an oblate Paul trap. The two structural states are (1) an open, hexagonal ring of ions and (2) a closed, pentagonal ring (with one ion in the center), as shown in figure 1.2. While only the closed-ring state is stable in a spherically-symmetric potential, the addition of an electric field that perturbs the rotationally-symmetric potential (what we will refer to as an anisotropic contribution to the trapping potential) has been shown to create a system in which both states correspond to stable local minima of the potential. It is in this state that the Campbell group has observed the structural transitions that we numerically analyze here.

Chapter 2

Relationship between the transverse-field Ising model and the XY model via the rotating-wave approximation

PLEASE NOTE: This chapter is a copy of the paper that Professor Freericks and I published earlier this year.

Abstract

In a large transverse field, there is an energy cost associated with flipping spins along the axis of the field. This penalty can be employed to relate the transverse-field Ising model in a large field to the XY model in no field (when measurements are performed at the right stroboscopic times). We describe the details for how this relationship works and, in particular, we also show under what circumstances it fails. We examine wavefunction overlap between the two models and observables, such as spin-spin Green's functions. In general, the mapping is quite robust at short times, but will ultimately fail if the run time becomes too long. There is also a trade-off between the length of time one can run a simulation out to and the time jitter of the stroboscopic measurements that must be balanced when planning to employ this mapping.

2.1 Introduction

Recently, there has been significant activity in employing the transverse-field Ising model within quantum simulators to examine adiabatic state preparation, excitation spectroscopy, quantum propagation speeds (Lieb-Robinson bounds) and complicated many-body phenomena like many body localization and time crystals [7, 8, 9, 10, 11, 12, 13, 14, 15, 16, 17]. The transverse-field Ising model is given by

$$\mathcal{H}_{TFI} = \sum_{i < j} J_{ij} \sigma_i^x \sigma_j^x - B \sum_i \sigma_i^z \quad (2.1)$$

where σ_i^α is the Pauli spin matrix at site i in spatial direction α . The spin-spin interactions are given by J_{ij} for the interaction between spins at sites i and j and will be called the spin-exchange piece of the Hamiltonian \mathcal{H}_{TFI}^{SE} , while the magnetic field strength in the z -direction is given by B (and the magnetic field piece of the Hamiltonian is denoted \mathcal{H}_{TFI}^B). In an adiabatic state preparation, the system would be initialized in a state polarized along the z -direction and then the field would be slowly reduced in the presence of the J_{ij} until the system evolved into the ground state of the Ising model with no field. If the system is evolved too rapidly, then diabatic excitations will occur, and their energies can be measured via different spectroscopy techniques. Lieb-Robinson bounds [18] can be inferred by measuring the propagation speeds of disturbances to the spin chain, while many body localization and time crystals require somewhat more sophisticated arrangements that include quasi disorder added to the system.

There also is an interest in going beyond the simple transverse-field Ising model to more complex systems. Here, one can imagine going to more complex spin models, like the XY model or the Heisenberg model, or one can imagine going to higher spin representations, like going to spin one instead of spin one-half. In this paper, we will focus on employing the rotating-wave approximation to go from the transverse-field Ising model to the XY model, which is given by the following Hamiltonian:

$$\mathcal{H}_{XY} = \frac{1}{2} \sum_{i < j} J_{ij} (\sigma_i^x \sigma_j^x + \sigma_i^y \sigma_j^y) \quad (2.2)$$

While it may not seem obvious, there is a rotating-wave approximation approach which will allow us to map the transverse-field Ising model into the XY model. We describe this next.

Define the spin raising and lowering operators via $\sigma^\pm = \sigma^x \pm i\sigma^y$. Inverting these relations lets us write $\sigma^x = (\sigma^+ + \sigma^-)/2$ and $\sigma^y = (\sigma^+ - \sigma^-)/2i$. A quick calculation then shows that $\sigma_i^x \sigma_j^x + \sigma_i^y \sigma_j^y = (\sigma_i^+ \sigma_j^- + \sigma_i^- \sigma_j^+)/2$. Thus, the XY model can be represented in terms of these raising and lowering operators. To find the relationship between the transverse-field Ising model and the XY model, we substitute the raising and lowering operators into the transverse-field Ising model in Eq. (2.1), by replacing σ^x by $(\sigma^+ + \sigma^-)/2$ everywhere. This yields

$$\mathcal{H}_{TFI} = \frac{1}{4} \sum_{i < j} (\sigma_i^+ \sigma_j^+ + \underbrace{\sigma_i^+ \sigma_j^- + \sigma_i^- \sigma_j^+ + \sigma_i^- \sigma_j^-}_{\text{XY piece}}) - B \sum_i \sigma_i^z. \quad (2.3)$$

Note how two of the spin-exchange terms are the same as those in the XY model, but there are two other operators which involve either raising the spins twice or lowering them twice. If the field B is large, there will be a large energy cost for those double spin flips, as opposed to having no energy cost for the XY terms which flip one spin up and the other spin down. This provides a hint that there should be a relationship between these two models in a large magnetic field.

To make the mapping more precise, we will invoke the rotating-wave approximation, which requires us to go to the interaction representation with respect to the magnetic field piece of the Hamiltonian (or, equivalently, to the rotating frame). We then transform the spin-exchange part of the Hamiltonian via $\mathcal{H}_{TFI}^{SE} \rightarrow \exp[i\mathcal{H}_{TFI}^B t] \mathcal{H}_{TFI}^{SE} \exp[-i\mathcal{H}_{TFI}^B t]$ to give us the interaction representation of the “perturbation.” In this rotating frame, the magnetic-field piece of the Hamiltonian is accounted for in the time dependence under the “unperturbed Hamiltonian” \mathcal{H}_0 , so the “interaction piece” of the transverse-field Ising model becomes

$$\mathcal{H}_{TFI} \rightarrow \frac{1}{4} \sum_{i < j} (\sigma_i^+ \sigma_j^+ e^{4iBt} + \sigma_i^+ \sigma_j^- + \sigma_i^- \sigma_j^+ + \sigma_i^- \sigma_j^- e^{-4iBt}). \quad (2.4)$$

When the magnetic field, B , is large, the rotating terms create rapidly oscillating terms in the Hamiltonian which average to zero and can be ignored via the rotating-wave approximation. So, whenever the rotating-wave approximation can be applied to the transverse-field Ising model, it should act like an XY model. To fully understand this mapping, though, we need to explore in detail how the energy eigenvalues relate as well as the dynamics of the

wavefunctions. In doing so, we will find the mapping holds stroboscopically in time because the frame is rotating at the Larmor frequency, and hence the wavefunctions have an oscillating phase which returns to a multiple of 2π every Larmor period. We will need to balance the improved accuracy given from a larger field with the difficulty in properly timing the stroboscopic measurements when the complex phase factors oscillate too rapidly.

In Sec. II, we derive the formalism we employ for making these comparisons. In Sec. III, we present results that illustrate both the success of the mapping and also show under what circumstances it fails. This is followed up by conclusions in Sec. IV.

2.2 Formalism

2.2.1 Spin Exchange Coefficients

In an ion trap, the internal ion states of a given atomic species are mapped onto the spins of a two-state system. A spin-dependent force is applied to the system, and in the situation where the phonons are only virtually created, they can be adiabatically eliminated from the system producing an effective spin-spin interaction. The spin-spin couplings vary with time, but their average values are given by [19]

$$J_{ij} = \Omega^2 \omega_R \sum_{m=1}^N \frac{b_{i,m} b_{j,m}}{\mu^2 - \omega_m^2}, \quad (2.5)$$

where Ω is the Rabi frequency, ω_R is the atomic recoil frequency, $b_{i,m}$ are the transverse phonon normal modes of the ion chain (labeled by the mode index m and the spatial position i), ω_m are the corresponding normal mode frequencies, and μ is the detuning frequency. The normal modes $b_{i,m}$ and normal-mode frequencies ω_m are found from a straightforward classical mechanics calculation once the trap parameters are known [20, 21]. The highest frequency transverse normal mode is the center-of-mass (COM) mode. When the detuning is larger than the COM mode frequency $\mu > \omega_{COM}$, the spin-exchange coefficients J_{ij} are well-approximated by a simple power law

$$J_{ij} \approx \frac{J_0}{|i-j|^\alpha}, \quad (2.6)$$

where α varies from 0 to 3 depending on the parameters of the Paul trap and the detuning. All frequencies in this paper that are expressed in units

of Hz are regular frequencies; the corresponding angular frequencies are 2π times larger. We use the trapping parameters of a recent experiments [12]: $\Omega\sqrt{\omega_R/\omega_{trans}} = 20$ kHz, $\omega_{trans} = 4.80$ MHz, and $\mu = \omega_{COM} + 60$ kHz, where ω_{COM} is the transverse center of mass phonon mode of the ion chain and is equal to ω_{trans} . We controlled the exchange coefficients by varying the anisotropy of the trap, that is, the ratio of the longitudinal to the transverse trapping frequency. We keep ω_{trans} fixed and vary ω_{lon} from 560 – 950 kHz, which yields an α varying between 0.63 and 1.19 with $J_0 \approx 500$ Hz.

2.2.2 Time Evolution

Both the transverse-field Ising model and the XY model are time-independent. The evolution operator is then given by $U(t) = \exp(-i\mathcal{H}t)$. If $U(t)$ is acting on a state that is not an energy eigenstate, then it is convenient to diagonalize the Hamiltonian in the exponential using V , a unitary matrix whose rows are the eigenvectors of \mathcal{H} , so that

$$U(t)|\Psi\rangle = V^\dagger e^{-iV\mathcal{H}V^\dagger t}V|\Psi\rangle. \quad (2.7)$$

Since we work in the same basis for both the transverse-field Ising model and the XY model, their respective evolution operators acting on a single initial state provides a direct comparison between the evolved states.

2.2.3 Energy Levels

Our first illustration of the mapping between these models involves a comparison of their energy levels. The transverse-field Ising model energy levels in a strong transverse field are approximately Zeeman shifted by $-2mB$, where m is the eigenvalue of the $S_{tot}^z = \sum_i \sigma_i^z/2$ operator. The shift is approximate because S_{tot}^z does not commute with the transverse-field Ising Hamiltonian. We identify approximate S_{tot}^z blocks in the transverse-field Ising energy levels in the limit of a large transverse field; that is, the energy levels will split based on the approximate value of S_{tot}^z acting on the corresponding eigenstate. Figure 2.1 shows the extent to which this is possible when $B/J_0 = 10$ in a 6-ion chain with $\omega_{lon} = 950$ kHz and $\alpha \approx 0.63$. The XY Hamiltonian commutes with the S_{tot}^z operator, so we can compare the energy states of both models on the basis of their S_{tot}^z value (approximate for the transverse-field Ising model and exact for the XY model).

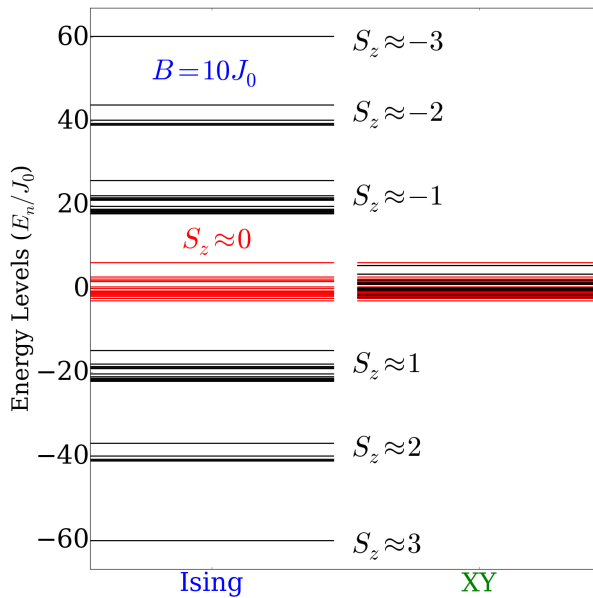


Figure 2.1: Energy levels of the transverse-field Ising Hamiltonian in a field of $B/J_0 = 10$ and of the XY Hamiltonian for a chain of 6 ions and a longitudinal trapping frequency of 950 kHz and $\alpha \approx 0.63$. The organization of the transverse-field Ising levels into approximate S_{tot}^z blocks is evident. The $S_{tot}^z \approx 0$ Ising levels and the $S_{tot}^z = 0$ XY levels are colored in red.

For systems with an even number of spin sites, we can directly compare the $S^z = 0$ energy levels of the XY model to the $S^z \approx 0$ Ising energy levels, as those levels are not Zeeman shifted to linear order in B .

The Ising energy levels in the limit of a large transverse field can be treated perturbatively, where the zero-field Ising Hamiltonian perturbs the transverse-field Hamiltonian. In a simultaneous eigenbasis of the S_{tot}^2 and S_{tot}^z operators, the magnetic-field-only Hamiltonian is highly degenerate. Fortunately, the zero-field Ising perturbation completely lifts the degeneracy. We diagonalize the S_{tot}^z blocks of the full transverse-field Ising Hamiltonian, and then sum over the contribution of other S_{tot}^z blocks to calculate the perturbative corrections. The second-order perturbative correction is given by

$$E_n^{(2)} = \sum_{m \neq n} \frac{\langle m | \mathcal{H}_{TFI}^{SE} | n \rangle \langle n | \mathcal{H}_{TFI}^{SE} | m \rangle}{E_n^0 - E_m^0}, \quad (2.8)$$

where E_n^0 is the unperturbed energy of the eigenstate $|n\rangle$ of \mathcal{H}_{TFI}^B . Second-order corrections to the energies of the $S_{tot}^z \approx 0$ block are all equal to zero. This indicates that the energies of the transverse-field Ising Hamiltonian are even functions of B , as the energies in the denominator are linear in B . The third-order correction, is then given by

$$\begin{aligned} E_n^{(3)} &= \sum_{m \neq n} \sum_{m' \neq n} \frac{\langle n | \mathcal{H}_{TFI}^{SE} | m \rangle \langle m | \mathcal{H}_{TFI}^{SE} | m' \rangle \langle m' | \mathcal{H}_{TFI}^{SE} | n \rangle}{(E_n^0 - E_{m'}^0)(E_n^0 - E_m^0)} \\ &\quad - \langle n | \mathcal{H}_{TFI}^{SE} | n \rangle \sum_{m \neq n} \frac{\langle m | \mathcal{H}_{TFI}^{SE} | n \rangle \langle n | \mathcal{H}_{TFI}^{SE} | m \rangle}{(E_n^0 - E_m^0)^2}, \end{aligned} \quad (2.9)$$

and is non-zero, which indicates that the $S_{tot}^z \approx 0$ Ising levels and $S_{tot}^z = 0$ XY levels should approach each other as $1/B^2$. Figure 2.2 shows the calculated energy differences at various field strengths, as well as a fit from the third-order perturbative correction, for a 6-ion chain with $\omega_{lon} = 950$ kHz ($\alpha \approx 0.63$).

For systems with an odd number of lattice sites, we need to shift the energy scales before comparing energy levels to account for the approximate Zeeman shift of a spin one-half state. Noting that S_{tot}^z commutes with the XY Hamiltonian, adding a transverse magnetic field to the XY model will result in Zeeman shifts that are exactly linear in the field strength. We therefore compare the transverse-field Ising energy levels with $\mathcal{H}_{XY}^{B \neq 0} = \sum_{i < j} \frac{J_{ij}}{2} (\sigma_i^x \sigma_j^x + \sigma_i^y \sigma_j^y) - B \sum_i \sigma_i^z$ when both models have an equal field strength. This comparison is shown visually in Fig. 2.3 for a 7-ion chain with $\omega_{lon} = 650$ kHz,

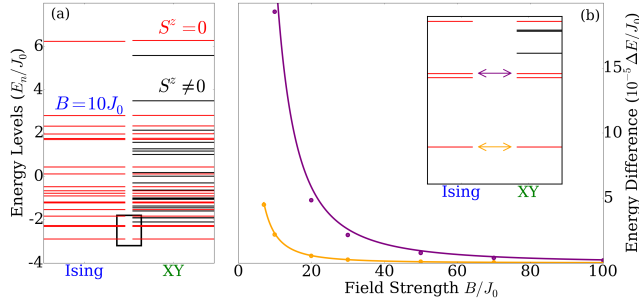


Figure 2.2: (a) Transverse-field Ising model energy levels for $B/J_0 = 10$ and XY model energy levels for a chain of 6 ions in a longitudinal trapping frequency of 950 kHz ($\alpha \approx 0.63$). Levels in the $S_{tot}^z \approx 0$ block of the Ising model and the $S_{tot}^z = 0$ block of the XY model are colored in red. (b) Difference between the corresponding XY and transverse-field Ising model energy levels is plotted as a function of field strength for $B/J_0 = 7, 10, 20, 30, 50, 70$, and 100. The particular levels used to measure the difference are shown in the inset with the arrows.

where the fit in panels (c) and (d) goes as $1/B$. Second-order perturbative corrections to transverse-field Ising blocks with $S_{tot}^z \neq 0$ are nonzero, which explains why the correction for $S_{tot}^z \neq 0$ blocks no longer go as $1/B^2$.

2.2.4 Wavefunction Overlap

A numerical evaluation of the modulus squared of the overlap between the XY and Ising wavefunctions as a function of time is shown in Fig. 2.4 for a 5-ion chain, $\omega_{lon} = 950$ kHz ($\alpha \approx 0.63$), and field strengths of $B/J_0 = 5, 10, 15$, and 20. The initial state for these calculations is the state with all spins oriented in the $-\hat{y}$ direction, which is represented in the z -basis as the direct-product state $|\Psi\rangle = (|\uparrow\rangle - i|\downarrow\rangle)_1 \otimes (|\uparrow\rangle - i|\downarrow\rangle)_2 \otimes \dots \otimes (|\uparrow\rangle - i|\downarrow\rangle)_N$. The black dots are placed at $2\pi n/\omega_L$, for integer n with $\omega_L = 4\pi B$, which corresponds to multiples of the Larmor period. The red dots are placed according to an optimized frequency, which is found by modifying the Larmor frequency from $4\pi B$ to $4\pi\sqrt{B^2 + (aJ_0)^2}$ and varying a until the combined sum of all modulus squares of the overlaps for a given range of times reaches a local maximum at integer multiples of the modified period. The form of the correction assumes that the spin-exchange interaction can be treated as a mean field in the \hat{x}

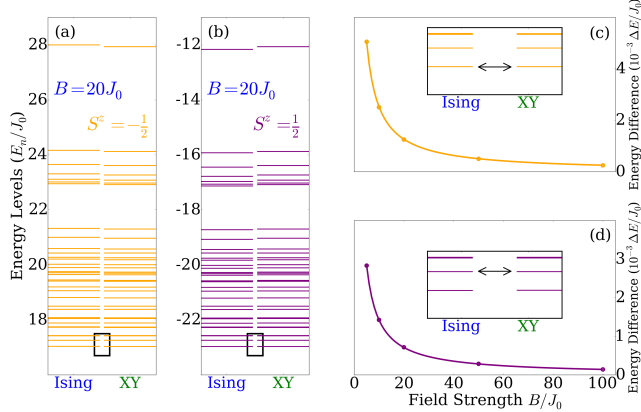


Figure 2.3: (a) XY and transverse-field Ising model energy levels for $S_{tot}^z = -\frac{1}{2}$ in an external field of $B/J_0 = 10$ on a chain of 7 ions with a longitudinal trapping frequency of 650 kHz ($\alpha \approx 1$). The $S_{tot}^z = \frac{1}{2}$ energy levels are plotted in panel (b). Panels (c) and (d) plot the field dependence of the difference between $S_{tot}^z = -\frac{1}{2}$ and $S_{tot}^z = \frac{1}{2}$ energy levels, respectively. The levels used to calculate the differences are identified in the inset by the arrows.

direction and that the frequency of the oscillations depends on the resultant magnitude of the total field. The corrected frequency in Fig. 2.4 corresponds to $a = 1.67$, which was determined by optimizing the sum of all plotted points between $tJ_0 = 0$ and $tJ_0 = 1$. In general, we found that a depends on the lattice size and on the initial state of the system, so it is not easy to know what it would be without solving the problem *a priori*. We went through this exercise to try to extend the period in time where the two models had wavefunctions that could be identified with each other stroboscopically. In general, however, if we don't have more accurate information available to us, we simply have to use the Larmor period, which breaks down a bit sooner than the corrected period.

The squared overlap oscillates between 1 and 0 at the Larmor frequency, while the envelope of the amplitude decays with time. The importance of the mean-field correction to the measurement frequency is shown clearly by the rapid rate of decay of the black dots relative to the red dots. Even for $B/J_0 = 20$, measurements taken with $\omega_L = 4\pi B$ will fall so far out of phase by $tJ_0 = 1$ that $|\langle \Phi_{Ising} | \Phi_{XY} \rangle|^2 \approx 0.5$, even though the state vectors are still coming into a maximum alignment of $|\langle \Psi_{Ising} | \Psi_{XY} \rangle|^2 \approx 0.9$ at slightly

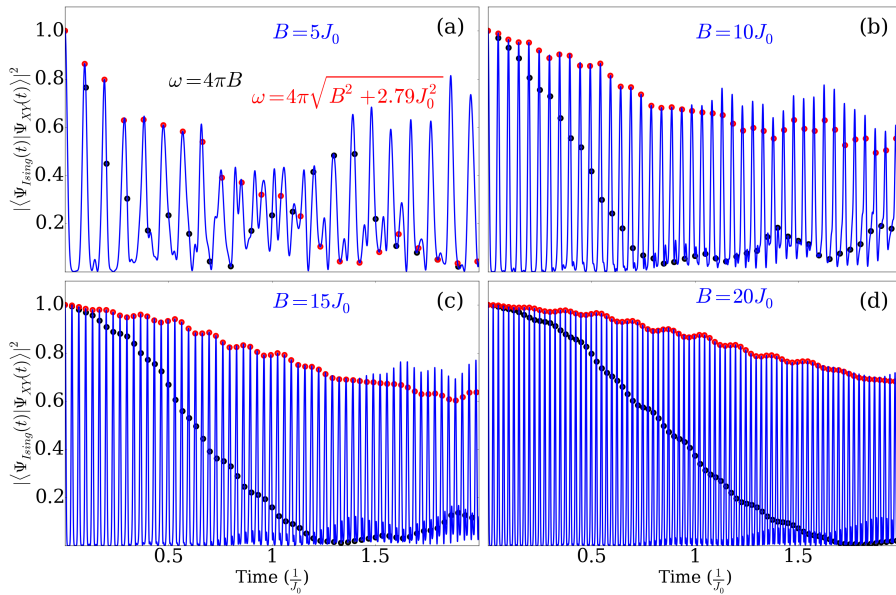


Figure 2.4: Plot of the modulus squared of the overlap of the time-evolved XY and transverse-field Ising state vectors, $\langle \Psi_{Ising}(t) | \Psi_{XY}(t) \rangle$, for a 5-ion chain with a longitudinal trapping frequency of 950 kHz ($\alpha \approx 0.63$) and various transverse field strengths. Panels (a)-(d) plot the squared overlap between $tJ_0 = 0$ and $tJ_0 = 2$ for $B/J_0 = 5, 10, 15$, and 20 , respectively. The black dots are plotted at the Larmor frequency, $\omega_L = 4\pi$. The red dots are plotted at a numerically-optimized frequency, given by $\omega_{opt} = 4\pi\sqrt{B^2 + (1.67J_0)^2}$.

different stroboscopic times.

2.2.5 Green's Function

We define the “pure-wavefunction” retarded spin-spin Green’s function via

$$G_{\alpha,\beta,i,j}^R(t, t_0) = i\theta(t - t_0)\langle \Psi_0 | [\sigma_i^\alpha(t), \sigma_j^\beta(t_0)] | \Psi_0 \rangle \quad (2.10)$$

where $\sigma_i^\alpha(t) = U^\dagger(t)\sigma_i^\alpha U(t)$ is a Pauli matrix in the Heisenberg picture. The equilibrium Green’s function (which would have a trace over all states rather than the pure-wavefunction definition above) can be easily shown to be invariant to translations in time, so that $G_{\alpha,\beta,i,j}^{Req}(t, t_0) = G_{\alpha,\beta,i,j}^{Req}(t+t', t_0+t')$. In the wave function form, this is only the case when $|\Psi_0\rangle$ is an eigenstate of the Hamiltonian. Since we cannot choose an initial state which is an eigenstate of both the XY and transverse-field Ising Hamiltonians, this definition of the pure-wavefunction retarded Green’s function is not always time-translation invariant. For transverse field strengths on the order of $10J_0$ and times on the order of $\frac{1}{J_0}$, however, deviations of this Green’s function from a time translation invariant one are negligible, so we ignore them. We choose to compare the $G_{x,x,i,j}^R$ components of the Green’s function because they can be measured experimentally with Ramsey spectroscopy [22, 23, 24].

In Fig. 2.5, we show the numerical evaluation of the $G_{x,x,0,1}^R(t, 0)$ for a 7-ion chain in the XY model and the transverse-field Ising model with $B/J_0 = 5, 10, 15$, and 20 and $\omega_{lon} = 650$ kHz ($\alpha \approx 1$). The pure state used in the Green’s function calculation is defined by $|\Phi_T\rangle = \sum_n \sqrt{\frac{\exp[-\beta E_n]}{Z}} |n\rangle$, where $Z = \sum_n \exp[-\beta E_n]$ and $\beta = \frac{2}{J_0}$. Note that this wavefunction is not a thermal state, but it is a linear combination of the eigenstates with the amplitudes of each state chosen to have the same probability as in a thermal state [25]. Dots indicate measurements of the transverse-field Ising model Green’s function at the particular times which correspond to the simulation of the XY model Green’s function. The red dots correspond to a mean field correction of $0.84J_0$ ($a = 0.84$) to the Larmor frequency (as discussed above), which was determined by optimizing the modulus squared of the overlap between XY and the transverse-field Ising evolutions of $|\Psi_T\rangle$ between $tJ_0 = 0$ and $tJ_0 = 1$.

The XY Green’s function initially traces the envelope of the fast-oscillating Ising Green’s function, but this relationship breaks down at around $tJ_0 = 0.9$. The dots do not reliably track the XY Green’s function until $B/J_0 = 15$, but even for $B/J_0 = 20$, the mapping falls off around $tJ_0 = 1$. Further, it

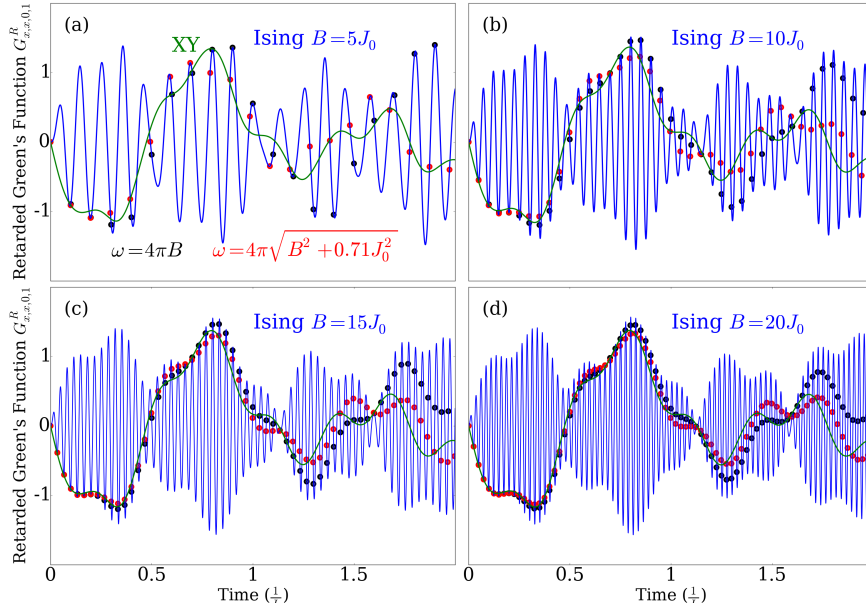


Figure 2.5: Plot of the pure-wavefunction retarded Green's function of the transverse-field Ising Hamiltonian, in blue, and of the XY Hamiltonian, in green, for a chain of 7 ions in a longitudinal trapping frequency of 650 kHz ($\alpha \approx 1$) and various transverse field strengths. Panels (a)-(d) plot the Green's functions between $tJ_0 = 0$ and $tJ_0 = 2$ for $B/J_0 = 5, 10, 15$, and 20 , respectively. The black dots are plotted at the Larmor frequency, $\omega_L = 4\pi$ and the red dots are plotted at a $\omega_{opt} = 4\pi\sqrt{B^2 + (0.84J_0)^2}$.

is important to note that the gradient of the transverse-field Ising model Green's function at measurement times increases with B because the XY curve does not simply follow its envelope. This means that experimental error will be amplified considerably in the presence of a large transverse field due to timing-jitter errors.

2.3 Results

The plots of the Green's function and of the wavefunction overlap indicate that there is an experimentally optimal field strength that would produce the most accurate simulation of the XY model for a given experimental error in data collection times. This optimal value is important because the slope of the oscillations of the transverse-field Ising model data at the times where data is collected can be huge. If we assume that an observable oscillates with $\nu \approx \nu_{Larmor} = 2B$, and that $J_0 \approx 400$ Hz, then the period of oscillation is $1.25 \times \frac{J_0}{B}$ milliseconds. A rough calculation of the optimal field strength can be made if we maintain that the experimental error in time measurements must be less than a tenth of the period of the observable. For experimental error of a microsecond, then, $B/J_0 \leq 125$, for example.

For fields of equal or lower magnitude than the optimal field strength, there are also maximum dephasing times, after which the overlap of the transverse-field Ising model evolved state and the XY evolved state will be too small to say that the two results are equivalent. Note also that the value of the overlap will differ depending on whether a simple Larmor frequency is used or whether a correction factor is included. Table I summarizes this dephasing time for the modulus squared of the overlap, defining the dephasing time as the time after which the squared overlap is less than 0.7.

This method of simulating an XY model evolution via the rotating-wave approximation has been used in an evaluation of Lieb-Robinson bounds for propagation speeds in systems with long-range correlations [12]. Their experiment used a Paul trap with $J_0 \approx 400$ Hz and a transverse field of $B/J_0 = 10$. They evaluate a static correlation function, $C_{i,j}(t) = \langle \sigma_i^y(t) \sigma_j^y(t) \rangle - \langle \sigma_i^y(t) \rangle \langle \sigma_j^y(t) \rangle$, between a spin on one end of an 11-site ion chain ($i = 0$) and all other spins in the chain. They also plot the evolution of this function up to $tJ_0 = 0.3$. In Fig. 2.6, we show a numerical evaluation of the same function for a longitudinal trapping frequency of 560 kHz corresponding to $\alpha \approx 1.19$. Their best fit Lieb-Robinson bound is also overlaid on those plots.

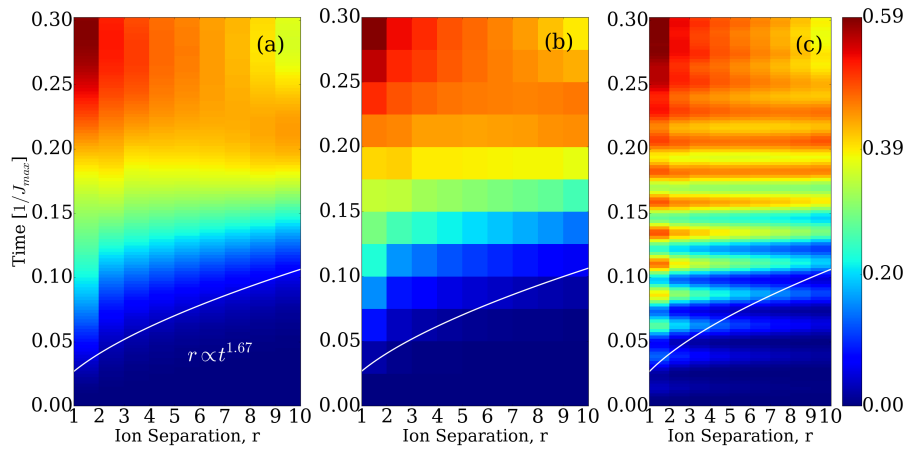


Figure 2.6: Color map for the spatiotemporal evolution of $C_{0,j}(t)$ on an 11-ion chain with a longitudinal trapping frequency of 560 kHz ($\alpha \approx 1.19$) and a field strength of $B/J_0 = 10$. Panel (a) plots the evolution of the XY model correlation function between $tJ_0 = 0$ and $tJ_0 = 0.3$. The white curve is a power law fit for the light cone of the correlations, reproduced from Ref. Panels (b) and (c) plot the evolution of the transverse-field Ising model, but (b) plots only the stroboscopic points with a sampling rate of twice the Larmor frequency, $2\omega_L = 8\pi B$. Panel (c) samples the system too frequently, so it does not produce the XY model accurately.

Field Strength (B/J_0)	Larmor Dephasing Time ($1/J_0$)	Optimal Dephasing Time ($1/J_0$)
5	0.20	0.28
10	0.35	0.79
15	0.50	1.29
20	0.63	1.79

Table 2.1: Dephasing time of the modulus squared of the overlap of the evolved XY and transverse-field Ising states, defined as the time at which $|\langle \Phi_{XY}(t) | \Phi_{Ising}(t) \rangle|^2 \leq 0.7$ compared to the strength of the transverse field. The data used to determine these values is the same as that presented in Fig. 2.4. The Larmor dephasing time corresponds to the black dots in Fig. 2.4, which are placed at a frequency of $\omega_L = 4\pi B$, and the corrected dephasing time corresponds to the red dots, placed at $\omega_{opt} = 4\pi\sqrt{B^2 + (1.67J_0)^2}$.

Panel (a) gives a numerical evolution of the correlation function for the XY model, while panels (b) and (c) show the transverse-field Ising simulation of the XY model. Panel (b) measures the transverse-field Ising model at the twice the Larmor frequency, which corresponds to the values for which this mapping occurs, while panel (c) measures the Ising model at a frequency eight times greater than the Larmor frequency (four times more frequent than the stroboscopic mapping, as detailed below). Note that the transverse-field Ising model, measured at the appropriate times, provides a good simulation of the XY model over this short timescale. This is not surprising for a field strength of $B/J_0 = 10$, given that the coherence time of the modulus squared of the overlap is $0.35/J_0$, or about 9 milliseconds for $J_0 \approx 400$ Hz. The white curve is the power law fit from the experiment. Note that imprecise timing would result in both a qualitatively different color map and an incorrect light cone measurement because the transverse-field Ising oscillations are nonnegligible compared to the features of $C_{i,j}(t)$, even at short timescales.

Note that the frequency used for the mapping of the correlation function $C_{i,j}(t)$ is $8\pi B$, which is twice that which is used for the overlap and the Green's function. This is because $C_{i,j}(t)$ is dependent upon the operator $\langle \sigma_i^y(t) \sigma_j^y(t) \rangle$. When the spins of the i th and j th ions have made one half rotation in the transverse field, which is oriented in the \hat{z} direction, $\langle \sigma_i^y(t_1) \rangle =$

$-\langle\sigma_i^y(t_0)\rangle$ and $\langle\sigma_j^y(t_1)\rangle = -\langle\sigma_j^y(t_0)\rangle$, so $\langle\sigma_i^y(t_1)\sigma_j^y(t_1)\rangle = \langle\sigma_i^y(t_0)\sigma_j^y(t_0)\rangle$. Thus, the mapping frequency for $C_{i,j}(t)$ is twice that of a quantity that depends on only one σ^α .

2.4 Conclusions

We examined the mapping between the transverse-field Ising model in a large magnetic field to the XY model in zero field via the rotating wave approximation. We compared the overlap of the wavefunctions for the two models, the time traces of a pure-state Green's function, and a static spin-spin correlation function. As the field in the Ising model is made larger, the mapping becomes more precise, but the oscillation frequency increases, so the measurement become more susceptible to timing jitter. In addition, objects like Green's functions map to each other only at the precise stroboscopic times, not at the envelope of their values, as occurs in other similar mappings. Finally, if one tries to follow this mapping for too long, it breaks down due to the imprecise mapping period (caused by a finite B field) and due to timing jitter in the measurements. Nevertheless, this mapping can be employed to perform simulations of the more complex XY model for short to intermediate times and is much simpler than directly simulating the full XY model. This approach has already been employed in quantum simulations. We hope our work helps quantify how far one can push this mapping, and more importantly, shows where it fails.

Chapter 3

Conformational Transition in Trapped-Ion Coulomb Crystal

In this chapter, I will present the work done on my second project regarding the analysis of a structural transition in a trapped-ion Coulomb crystal. The first two sections of this chapter are Computational Simulation, in which I will present my methods for modeling the Coulomb crystal and possible transition pathways, and Data Analysis, in which I will address the methods I used to interpret experimental data taken by the Campbell group and the results of that work. Ideally, this chapter would conclude with a section comparing the results of the two analyses. Unfortunately, however, the trapping parameters that the Campbell group originally gave to us did not correspond to the measurements they had taken of the system as it transitions. They are in the process of sending us matching data and parameters, but they have run into technical difficulties, so that information will not arrive in time to be included in this thesis. I have attempted to generate potential surfaces that correspond to the data we have, using a method that I will discuss in the first section of this chapter, but they are merely guesses and should not be assumed to be accurate. The final section of this chapter, Conclusions, therefore serves as an explanation of what my analysis has shown so far and what we hope to be able to do when we receive matching data and trapping parameters.

3.1 Computational Simulation

We are analyzing a Coulomb crystal generated by Dr. Wes Campbell and his group at UCLA. Their experimental configuration consists of an oblate Paul trap that confines six $^{171}\text{Yb}^+$ ions to a two-dimensional plane. The potential within the plane squeezes the ions radially inward, and the Coulomb crystal is the geometry that minimizes the potential energy of the system (balancing the mutual repulsion between ions and the trapping potential). The Campbell group has also added a term to the potential energy that breaks the rotational symmetry, which has been shown to create a system in which both the open and closed ring states correspond to local minima of the net potential [3].

Using the gradient of the potential energy, we can determine the classical path that the ions will follow from arbitrary initial arrangements into the optimized positions. That said, determining a potential barrier that the ions must overcome to move from one structural state to another is nontrivial because the potential is defined in twelve-dimensional space (assuming that the ions can only move within the plane of the trap). Using computational simulations of the transition, we have been able to define the potential barrier and determine the thermally-activated rate of transition across it as well as the probability of quantum tunneling.

3.1.1 Derivation of the Oblate Paul Trap Potential

The derivation of the Oblate Paul trap potential is presented originally in Yoshimura et al. [3]. I will present a consensed version of this derivation that differs only in the specific values of the experimental parameters. I will also discuss the nature of an anisotropic, or “symmetry-breaking,” contribution to the potential.

A Paul trap consists of two DC end-cap electrodes which sit above and below a central RF ring. According to Earnshaw’s theorem, a static electric field cannot create local minima or maxima in free space. This can be understood intuitively using Gauss’ Law: the divergence of the electric force at a local minimum should be negative (and at a local maximum it should be positive), but Gauss’ Law says that $\vec{\nabla} \cdot \vec{F} = 0$ in a space without free charges. Thus, a static electric field can only create saddle points in free space.

The Paul trap, so described, creates such a saddle point at the center of the RF ring. In order to confine ions in all spatial directions, a time-varying

voltage is applied to the electrodes such that the saddle point oscillates sinusoidally as a function of time. As long as ion micromotion is small and slow with respect to the frequency of oscillation of the potential, then the resulting potential may be described by a static pseudopotential. The shape of this potential has been determined through a Comsol simulation, and can be written as

$$\tilde{V}(\tilde{x}_1, \tilde{x}_2, \tilde{x}_3) = \psi(\tilde{x}_1, \tilde{x}_2, \tilde{x}_3) + q\phi(\tilde{x}_1, \tilde{x}_2, \tilde{x}_3)$$

where $\psi = \frac{q^2 V_{0,RF}^2}{m\Omega_{RF}^2 r_0^4} (\tilde{x}_1^2 + \tilde{x}_2^2 + 4\tilde{x}_3^2)$ is the RF contribution and ϕ is the DC contribution. The latter may be broken up into three terms: the DC voltage on the RF ring, $\phi_r = \frac{V_r}{r_0^2} (\tilde{x}_1^2 + \tilde{x}_2^2 - 2\tilde{x}_3^2)$, and the DC voltage on the top and bottom endcaps, $\phi_{t,b} = V_{t,b} \left(\frac{\tilde{x}_3^2}{a^2} + \frac{\tilde{x}_3}{b_{t,b}} - \frac{\tilde{x}_1^2 + \tilde{x}_2^2}{c^2} + d \right)$. The relevant parameters that we used are the amplitude of the RF voltage, $V_{0,RF} = 320$ V, the RF frequency, $\Omega_{RF} = 2\pi \times 48.484$ MHz, the DC voltage on the ring, $V_r = 5$ V, the DC voltage on the top endcap, $V_t = 4$ V, the DC voltage on the bottom endcap, $V_b = 4$ V, and the geometric fitting parameters, derived from the Comsol simulation: $a = 524$ μm, $b_t = 761$ μm, $b_b = -761$ μm, $c = 704$ μm, $d = 0.812$, and $r_0 = 512$ nm.

The conventional way to write the net potential energy of an oblate Paul trap is in terms of harmonic oscillator frequencies. For the trap used by the Campbell group, this is given by

$$\begin{aligned} \tilde{V} = \frac{1}{2}m[\sum_{i=1}^2(\omega_{\psi,i}^2 + \omega_{r,i}^2 - \omega_{b,i}^2 - \omega_{t,i}^2)\tilde{x}_i^2 + \omega_{\psi,3}^2\tilde{x}_3^2 - \omega_{r,3}^2\tilde{x}_3^2 + \\ + \omega_{t,3}^2(\tilde{x}_3 + \frac{a}{2b_t})^2 + \omega_{b,3}^2(\tilde{x}_3 + \frac{a}{2b_b})] + \frac{1}{2}\sum_{m \neq n}^N \frac{k_e e^2}{\tilde{r}_{m,n}}, \quad (3.1) \end{aligned}$$

where

$$\omega_{\psi,1} = \frac{\sqrt{2}qV_{0,RF}}{m\Omega_{RF}r_0^2} = \omega_{\psi,2} = \frac{\omega_{\psi,3}}{2},$$

$$\omega_{r,1} = \sqrt{\frac{2qV_r}{mr_0^2}} = \omega_{r,2} = \frac{\omega_{r,3}}{\sqrt{2}},$$

$$\omega_{b,1} = \sqrt{\frac{2qV_b}{mc^2}} = \omega_{b,2} = \frac{a}{c}\omega_{b,3},$$

and $\omega_{t,i}$ is given by the equation for $\omega_{b,i}$ with V_b replaced by V_t . Going forward, we will express the distance between ions in the trap in terms of a characteristic length scale, $l_0 \equiv (\frac{k_e e^2}{m\omega_{\psi,3}^2})^{1/3}$. Normalized distances are given by $x \equiv \tilde{x}/l_0$. We also express all frequencies in terms of $\omega_{\psi,3}$. Normalized frequencies are given by

$$\beta_i = \frac{1}{\omega_{\psi,3}} \sqrt{\omega_{\psi,i}^2 + \omega_{r,i}^2 - \omega_{b,i}^2 - \omega_{t,i}^2}$$

for $i = 1, 2$, $\beta_{r,3} = \omega_{r,3}/\omega_{\psi,3}$, $\beta_{b,3} = \omega_{b,3}/\omega_{\psi,3}$, and $\beta_{t,3} = \omega_{t,3}/\omega_{\psi,3}$. The potential can then be expressed in dimensionless form as

$$V = \frac{\tilde{V}}{k_e e^2 / l_0} = \frac{1}{2} \sum_{n=1}^N [\beta_1^2 x_{1,n}^2 + \beta_2^2 x_{2,n}^2 + x_{3,n}^2 - \beta_{r,3}^2 x_{3,n}^2 + \beta_{t,3}^2 (x_{3,n} + x_{o,t})^2 + \beta_{b,3}^2 (x_{3,n} + x_{o,b})^2] + \frac{1}{2} \sum_{m \neq n}^N \frac{1}{r_{nm}}, \quad (3.2)$$

where $x_{o,t} = a^2/(2l_0 b_t)$ and $x_{o,b} = a^2/(2l_0 b_b)$. The gradient of this potential is given by

$$\nabla V = \sum_{m=1}^N \left[\sum_{i=1}^2 \hat{e}_{i,m} \beta_i^2 x_{i,m} + \hat{e}_{3,m} [x_{3,m} - \beta_{r,3}^2 x_{3,m} + \beta_{t,3}^2 (x_{3,m} + x_{o,t}) + \beta_{b,3}^2 (x_{3,m} + x_{o,b})] + \sum_{n \neq m}^N \sum_{i=1}^3 \hat{e}_{i,m} \frac{x_{i,n} - x_{i,m}}{r_{nm}^3} \right]. \quad (3.3)$$

The ions must all be confined to the $\hat{e}_1 - \hat{e}_2$ plane in the oblate Paul trap, so we are only looking for solutions for which $x_{3,m} = \bar{x}_3 \forall m \in [1, N]$. We also want the \hat{e}_3 component of the force on each ion to be zero, so $\nabla V \cdot \hat{e}_{3,m} = 0 \forall m \in [1, N]$. It is then trivial to solve for \bar{x}_3 , which is given by

$$\bar{x}_3 = \frac{-\beta_{t,3}^2 x_{o,t} - \beta_{b,3}^2 x_{o,b}}{1 - \beta_{r,3}^2 + \beta_{b,3}^2 + \beta_{t,3}^2}.$$

We can then expand this potential around the equilibrium positions, found by setting $\nabla V|_{eq} = 0$, which gives us

$$V = V^{(0)} + \frac{1}{2} \sum_{i,j=1}^3 \sum_{m,n=1}^N q_{i,m} q_{j,n} \frac{\partial^2 V}{\partial x_{i,m} \partial x_{j,n}}|_{eq}.$$

Note that the $q_{i,n}$ is the dimensionless displacement in the \hat{e}_i direction from the equilibrium position of ion n . I will define the dimensionless equilibrium coordinates as those having a bar over them, such as $\bar{x}_{i,n}$. The dimensionless Lagrangian can therefore be written as

$$L = \frac{1}{2\omega_{\psi,3}^2} \sum_{i=1}^3 \sum_{m=1}^N \dot{q}_{i,m}^2 - \frac{1}{2} \sum_{i,j=1}^3 \sum_{m,n=1}^N q_{i,m} K_{mn}^{ij} q_{j,n}, \quad (3.4)$$

where $K_{mn}^{ij} = \frac{\partial^2 V}{\partial x_{i,m} \partial x_{j,n}}$ is an element from the effective spring constant matrices. For $(i, j) \in [1, 2]|i \neq j$, this is given by

$$K_{mn}^{ii} = \begin{cases} \beta_i^2 - \sum_{n' \neq m}^N \left[\frac{1}{\bar{r}_{n'm}^3} - 3 \frac{(\bar{x}_{i,n'} - \bar{x}_{i,m})^2}{\bar{r}_{n'm}^5} \right] & \text{if } m = n \\ \frac{1}{\bar{r}_{nm}^3} - 3 \frac{(\bar{x}_{i,n} - \bar{x}_{i,m})^2}{\bar{r}_{nm}^5} & \text{if } m \neq n \end{cases} \quad (3.5)$$

$$K_{mn}^{ij} = K_{mn}^{ji} = \begin{cases} 3 \sum_{n' \neq m}^N \frac{(\bar{x}_{i,n'} - \bar{x}_{i,m})(\bar{x}_{j,n'} - \bar{x}_{j,m})}{\bar{r}_{n'm}^5} & \text{if } m = n \\ -3 \frac{(\bar{x}_{i,n} - \bar{x}_{i,m})(\bar{x}_{j,n} - \bar{x}_{j,m})}{\bar{r}_{nm}^5} & \text{if } m \neq n \end{cases} \quad (3.6)$$

The \hat{e}_3 direction is completely decoupled from the $\hat{e}_1 - \hat{e}_2$ plane, so the only non-zero components of K_{mn}^{ij} in the \hat{e}_3 direction are given by

$$K_{mn}^{33} = \begin{cases} \beta_3^2 - \sum_{n' \neq m}^N \frac{1}{\bar{r}_{n'm}^3} & \text{if } m = n \\ \frac{1}{\bar{r}_{nm}^3} & \text{if } m \neq n \end{cases} \quad (3.7)$$

where $\beta_3^2 \equiv 1 - \beta_{r,3}^2 + \beta_{t,3}^2 + \beta_{b,3}^2$. By applying the Euler-Lagrange condition to equation 3.4, and assuming that the eigenvalues satisfy $q_{i,m} = Re(b_{i,m}^\alpha e^{i\omega_\alpha t})$, we can now solve for the normal modes about equilibrium ion positions:

$$-b_{i,m}^\alpha \left(\frac{\omega_\alpha}{\omega_{\phi,3}} \right)^2 + \sum_{j=1}^3 \sum_{n=1}^N K_{mn}^{ij} b_{i,m}^\alpha. \quad (3.8)$$

Anisotropic Contribution

The potential surface of the oblate Paul trap, as it has been described so far, is rotationally symmetrical. This means that, in an equilibrium configuration of ions in this potential, there will exist a zero-frequency rotational mode. In other words, the equilibrium positions of the ions are infinitely degenerate because any rotation about the center of the trap will yield another, equivalent equilibrium configuration.

The introduction of a single symmetry-breaking potential resolves this problem, resulting in a finite degeneracy of equilibrium ion positions. Furthermore, the Campbell group has found that the introduction of such a potential can create a potential surface in which there are two stable local minima. The potential that they use is given by

$$\phi_{aniso} = \frac{qV_c}{r_0^2}(x_1^2 - x_2^2), \quad (3.9)$$

where V_c is the voltage parameter that can be used to control the strength of this contribution. The associated frequency is $\omega_{aniso} = \sqrt{2qV_c/mr_0^2}$. Following the same procedure used to arrive at equation 3.1, we can see that the addition of the symmetry-breaking potential to the oblate Paul trap simply results in a modification to β_1 and β_2 in equation 3.2:

$$\begin{aligned} \beta_1 &= \frac{1}{\omega_{\psi,3}} \sqrt{\omega_{\psi,i}^2 + \omega_{r,i}^2 - \omega_{b,i}^2 - \omega_{t,i}^2 + \omega_{aniso}^2} \\ \beta_2 &= \frac{1}{\omega_{\psi,3}} \sqrt{\omega_{\psi,i}^2 + \omega_{r,i}^2 - \omega_{b,i}^2 - \omega_{t,i}^2 - \omega_{aniso}^2} \end{aligned}$$

It is worth restating that the addition of a symmetry-breaking potential results in a finite degeneracy of equilibrium states. There is still a non-zero degeneracy of equilibrium states after the addition of ϕ_{aniso} based on the axes of symmetry of the net trapping potential.

3.1.2 Transition State Theory

Classical transition state theory gives a simple formula for the rate at which particles in a metastable state travel over a potential barrier. This formula is based on the Arrhenius equation, in which the rate is proportional to the Arrhenius factor, $\exp -\beta E_b$ (note that E_b is the height of the energy barrier). The constant of proportionality of a particle escaping from a one-dimensional

well is just equal to the curvature at the bottom of the well, $\omega_0/2\pi$. This equation can be generalized for application to many-body systems,

$$\Gamma = \nu^* \exp -\beta E_b,$$

by defining an average frequency, ν^* , equal to the product of all eigenfrequencies of the local minimum divided by the product of all stable eigenfrequencies of the maximum energy state:

$$\nu^* = \frac{\prod_{j=1}^N \nu_j^0}{\prod_{j=1}^{N-1} \bar{\nu}_j}.$$

Note that the maximum energy state along the path between local minima must be a one-dimensional saddle point so that Γ has units of frequency. Many-body rate theory makes two key assumptions: (1) that the entire system remains in thermodynamic equilibrium throughout the transition, and (2) that particles that have traversed the boundary cannot return [26]. The second assumption may be reasonable for very low temperatures, given that the state from which the system transitions is metastable (i.e. that its energy is higher than that of the other local minimum). The first assumption, however, is harder to accept. In order to assume that the system remains in an equilibrium state throughout the transition, we must imagine that the time it takes the particle to achieve thermal equilibrium within a potential well is much shorter than the timescale on which it transitions between wells. In many cases, one or both of these assumptions are unreasonable. For that reason, we present this formula as a first-order approximation of the transition rate between states.

3.1.3 Minimum Energy Path (MEP)

The minimum energy path is the path from one local minimum of the potential energy to another such that any point on the path is an energy minimum in all directions perpendicular to the path at that point [28]. It is therefore necessary that the maximum energy state along this path be a first-order saddle point, as that point will be a maximum of the energy along the direction of the path and a minimum of the energy in all other directions. This can be thought of as the path taken by a classical particle with zero kinetic energy (i.e. that has no momentum and no velocity after every step), and it

corresponds to the lowest possible potential energy barrier between the local minima.

We want to identify the minimum energy path because it will give us a definitive lower bound on the energy barrier between states. While it may be unrealistic to assume that the system actually transitions between states along the MEP, it is useful insofar as it serves as an ideal case for a thermally-activated transition. Furthermore, the maximum energy state along the MEP is a saddle point, and therefore can be used to calculate the rate of thermally-activated transitions between states according to equation 3.1.2.

Approximating the Energy Barrier

The MEP between two local minima of a twelve-dimensional potential is by no means obvious. It is therefore efficient and often fruitful to construct simplified guesses at the MEP in order to learn more about the potential barrier between local minima. We used three such methods, which I will present in order of increasing sophistication.

The simplest method is to imagine a path that minimizes the distance traveled in twelve-dimensional space. Visually, this amounts to drawing a straight line between the starting position (in one local minimum) of each ion and its ending position (in the other local minimum). The choice of which ion in the starting configuration moves to a given position in the final configuration is chosen such that the net distance travelled by all ions is minimized. The path of each ion is broken up into an equal number of evenly-sized steps, which allows us to construct a trajectory in twelve-dimensional space. The transition in the plane of the Paul trap is shown in figure 3.1, as well as the energy of the system at each point along the trajectory as a function of the total distance travelled by all ions. The energy barrier generated will overestimate the actual energy barrier, but can be used as an order-of-magnitude approximation. Furthermore, such a trajectory may be close to the actual pathway for a quantum transition, for which the probability of traversing the boundary decays exponentially with distance traveled.

A more accurate approximation of the energy barrier may be obtained via the drag method. This consists of dragging one ion from its position in the first minimum configuration to a position in the second minimum configuration and allowing all the other ions to “relax” around it after each

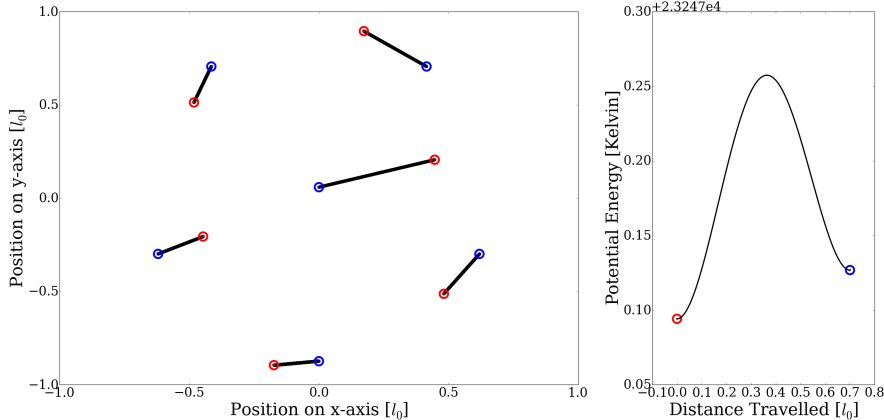


Figure 3.1: The most basic approximation of the transition pathway between states. The left panel shows the pathway of the six ions in the plane of the oblate Paul trap. The right panel shows the energy of the system at each point along the path. The red dots correspond to the hexagonal state and the blue dots correspond to the pentagonal state.

step. The challenge with implementing this method is that the ion being dragged must cause the transition between states. Choosing, for example, an ion in the hexagonal ring and dragging it to a nearby position on the ring of the pentagonal configuration will not bring the entire system into the basin of attraction around the pentagonal configuration; more specifically, such a choice would not cause any of the other ions to move into the center of the ring. The most simple choice to cause a transition into the pentagonal state is to drag one of the ions in the hexagonal ring to the origin. We begin by constructing a linear trajectory with equally-sized steps for the ion being dragged. After this ion is dragged a single step, it is fixed in that position and the remaining ions are allowed to relax into a new minimum-energy configuration around it. This process is repeated until the system arrives at the second local minimum configuration. For this method to give practical results, the step size must be small so that the other ions follow continuous paths. The resulting energy barrier, shown in figure 3.2, is still an overestimation of the true energy barrier. It is, however, a much more realistic approximation that can be used for rate calculations of both quantum and classical transitions.

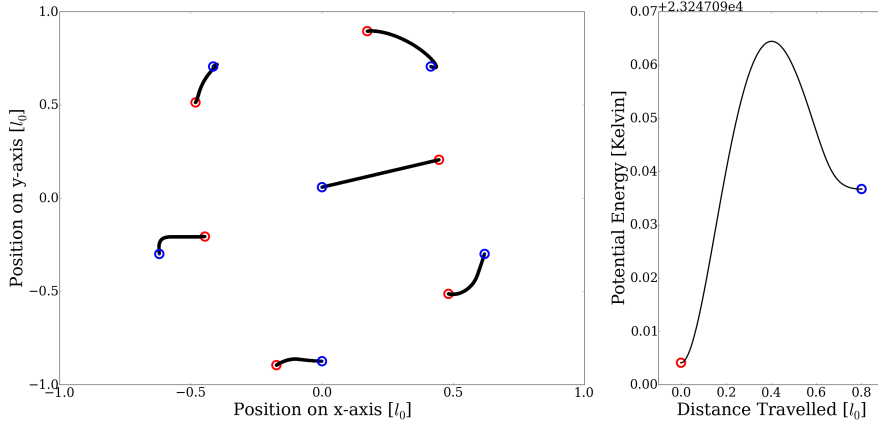


Figure 3.2: The result of the drag method approximation of the transition pathway between states. The left panel shows the pathway of the six ions in the plane of the oblate Paul trap. The right panel shows the energy of the system at each point along the path. The red dots correspond to the hexagonal state and the blue dots correspond to the pentagonal state.

The most sophisticated and accurate approximation of the energy barrier that we used was obtained via the nudged elastic band (NEB) method. This method begins with an initial guess at the trajectory between local minima. This guess may be as simple as that which was obtained by the first method, but the NEB method was more efficient in our experience when using the drag method trajectory as the initial guess. For the purposes of this explanation, I will define an initial trajectory of size n as one that has $n - 2$ intermediate states between the local minima, and I will number those states such that 1 refers to the first local minimum and n refers to the second local minimum. We begin by defining a new potential energy function,

$$V_{NEB} = \sum_{i=2}^{n-1} V_i + \sum_{i=1}^{n-1} U_{i,i+1}^{spring}, \quad (3.10)$$

which consists of the sum of the potential energy of each intermediate state of the trajectory as well as the sum of a set of spring terms. These latter terms can be thought of the potential energy of a hypothetical spring that connects each ion with its corresponding position in the next step of the trajectory. The significance of this term can be understood by thinking

of the entire trajectory as an elastic band with fixed endpoints that is being stretched and shaped by the contours of the underlying potential. The “nudging” of this elastic band consists of removing projections of the potential gradient that will cause unwanted features in our final trajectory, namely “slipping” (where the direction of the spring force causes a trajectory to slip off the MEP into a region of higher energy) and “sliding” (where the gradient of the first term of V_{NEB} causes the points of the trajectory to bunch up around the local minima). The resulting potential gradient is given by

$$\nabla V_{NEB} = \sum_{i=2}^{n-1} \{ [\nabla V_i - \nabla V_i \cdot \hat{\tau}_i] + [\nabla U_{i,i+1}^{spring} - \nabla U_{i-1,i}^{spring}] \cdot \hat{\tau}_i \}, \quad (3.11)$$

where $\hat{\tau}_i$ is the unit tangent to the path. We estimated this direction in accordance with reference [27]. The final step in the NEB method is to minimize the energy of the trajectory with respect to V_{NEB} , making use of ∇V_{NEB} as the jacobian. Nudging the trajectory in this way should give us a final trajectory that is smooth and has evenly-spaced points. This is borne out for the majority of the path in figure 3.3, with the exception of the area surrounding the maximum of the path. We believe this to be due to the numerical minimization protocol we used, as this was not the case for all paths calculated using the NEB method.

In general, we found that the energy barrier found via the NEB method is a very good approximation of the actual energy barrier. In principle, the NEB trajectory should converge on the minimum energy path, but our minimization protocol was never powerful enough to realize precise convergence [27].

Arriving at the MEP

Making use of the reliability of the NEB trajectory in approximating the MEP as well as the fact that the maximum energy state along the MEP must be a first-order saddle point, we have been able to numerically solve for the MEP. The first step in this method is to identify the configuration of ions that corresponds to the maximum energy state along the NEB trajectory. The simplicity of our model and the fidelity of the NEB method have allowed us to reliably assume this state to have a single unstable mode. We are therefore able to find the saddle point of the potential by maximizing the potential energy along the direction given by the unstable eigenvector and minimizing

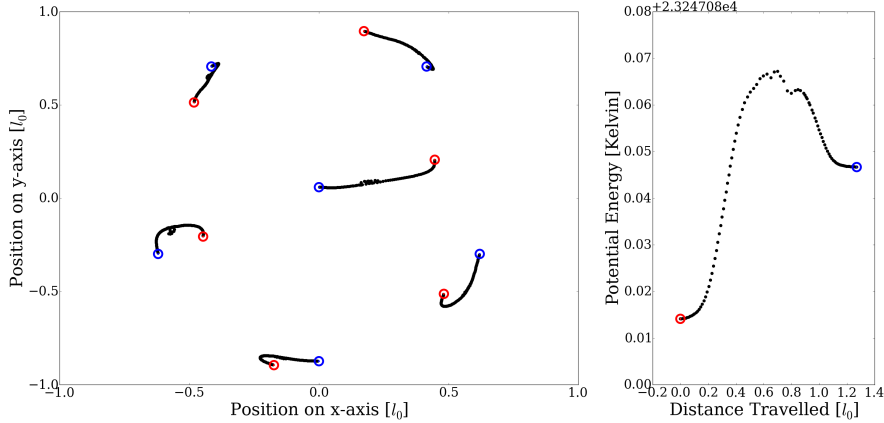


Figure 3.3: The result of the nudged elastic band (NEB) approximation of the transition pathway between states. The left panel shows the pathway of the six ions in the plane of the oblate Paul trap. The right panel shows the energy of the system at each point along the path. The red dots correspond to the hexagonal state and the blue dots correspond to the pentagonal state.

the potential with respect to all other stable eigenvectors. We perform this optimization protocol twice in order to ensure that the position is precise. This is the maximum energy state of the MEP.

From the saddle point, the full MEP can be obtained by a two-part process: (1) stepping in the direction opposite the component of the gradient that is parallel to the unstable eigenvector until the system enters a region in which there are no unstable eigenvectors, and (2) following Newton's method of gradient descent, in which steps of magnitude $\frac{|\nabla V(p)|^2}{\nabla V(p) \cdot H(p) \cdot \nabla V(p)}$ are taken in the direction opposite the gradient of a point p . Note that $\nabla V(p)$ and $H(p)$ refer to the gradient of the potential evaluated at point p and the Hessian matrix evaluated at point p , respectively. The reason that this method is divided into two steps is that Newton's method only converges on a local minimum when the Hessian matrix is positive definite (i.e. $z^T H z$ is positive for any non-zero vector z that contains only real numbers), so a modified version of gradient descent must be used until this condition is achieved. The resulting path is shown in figures 3.4 and 3.5.

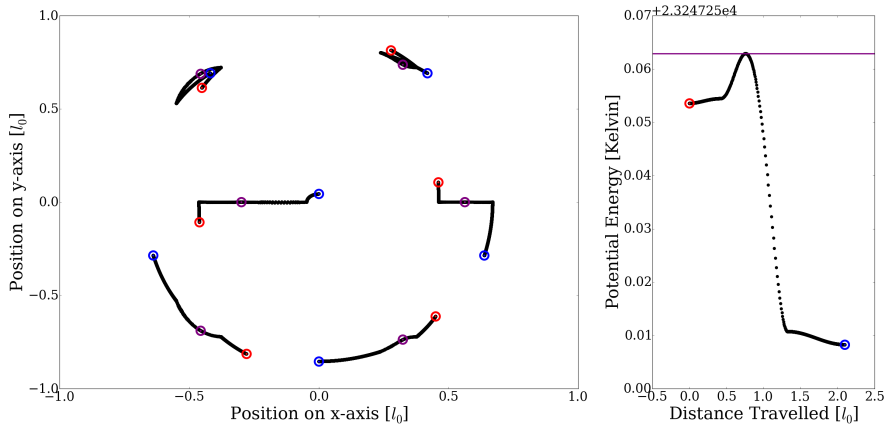


Figure 3.4: The calculated minimum energy path (MEP) for trapping parameters corresponding to $M2=9$. The left panel shows the calculated minimum energy path (MEP) between the hexagonal and pentagonal states in the plane of the oblate Paul trap. The purple dots correspond to the saddle point, which is also the maximum energy state along the MEP. The right panel shows the energy of the system at each point along the path, and the saddle point energy is given by the horizontal purple line. The red dots correspond to the hexagonal state and the blue dots correspond to the pentagonal state.

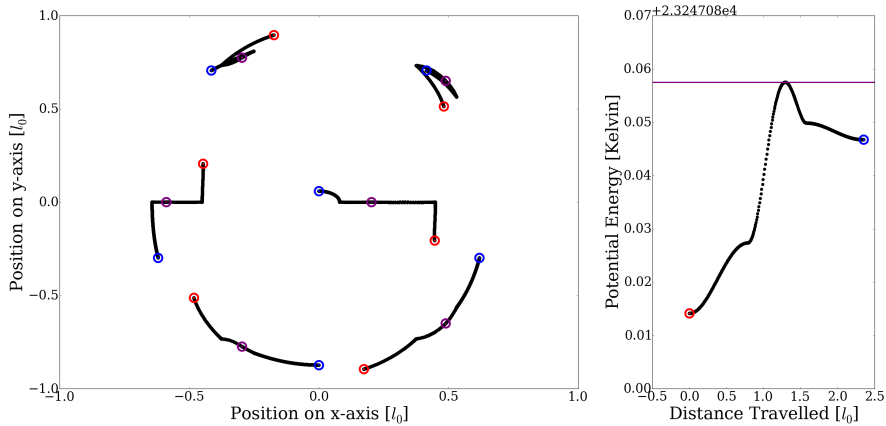


Figure 3.5: The calculated minimum energy path (MEP) for trapping parameters corresponding to $M2=10$. The left panel shows the calculated minimum energy path (MEP) between the hexagonal and pentagonal states in the plane of the oblate Paul trap. The purple dots correspond to the saddle point, which is also the maximum energy state along the MEP. The right panel shows the energy of the system at each point along the path, and the saddle point energy is given by the horizontal purple line. The red dots correspond to the hexagonal state and the blue dots correspond to the pentagonal state.

3.1.4 Results

As we mentioned at the beginning of this chapter, we have not yet received accurate parameters corresponding to the data presented in the first section. In order to present the overlap between theoretical and experimental analyses, however, we attempted to generate parameters that roughly correspond to the data sets. We did this by generating 1000 random initial states for a given value of V_c and running a minimization protocol on each. From this data, we were able to calculate the percentage of initial states that would minimize to the hexagonal state. We then tried to match this to the percentage of time that the Campbell group's system was in the hexagonal state for each plot ($M2=9$, $M2=10$, and $M2=11$) in figure 3.6. It is worth noting that our method gave percentages that are indicative of the relative sizes of the potential basins (the “volume” of 12-dimensional space in which the system will minimize to one of the local minima) for each state, whereas the percentage of time spent in each state during the experiment is theoretically dependent on the relative sizes and depths of the potential basins as well as the mode of transition across the energy barrier. We have no reason to draw an equivalence between these two percentages, so we are not presenting them as results of any serious analysis. The choice to match potentials in this manner was due to the fact that it did not require us to presume a particular method of transition across the potential barrier.

The values of the spherically asymmetrical voltage in equation 3.9 for $M2=9$, $M2=10$, and $M2=11$ are $V_c = 0.4929$ V, $V_c = 0.5763$ V, and $V_c = 0.6306$ V, respectively. These values correspond to percentages of 0.368, 0.513, and 0.993, respectively, in the hexagonal state.

Classical Transition

The calculated MEP for the parameters corresponding to $M2=9$ is shown in figure 3.4, and the MEP for parameters corresponding to $M2=10$ is shown in figure 3.5. We were unable to construct a minimum energy path for the parameters corresponding to $M2=11$ because the analysis described above led us to a set of parameters in which the pentagonal state is a saddle point. This appears to be consistent with the third panel of figure 3.6, as the system never enters into a second stable state.

It is clear from figures 3.4 and 3.5 that a thermally-excited system could not follow these MEPs exactly. This is because the MEP is the path that

	M2=9	M2=10
$E_b^{P \rightarrow H}$ [K]	5.46×10^{-2}	1.08×10^{-2}
$\nu_{P \rightarrow H}^*$ [kHz]	811	997
$\omega_0^{P \rightarrow H}/2\pi$ [kHz]	98	229
$\Gamma_{P \rightarrow H}$ (T=1 mK) [Hz]	1.51×10^{-18}	2.03×10^2
$\Gamma_{P \rightarrow H}$ (T=5 mK) [Hz]	1.45×10^{-3}	1.15×10^5
$E_b^{H \rightarrow P}$ [K]	9.35×10^{-3}	4.34×10^{-2}
$\nu_{H \rightarrow P}^*$ [kHz]	704	2380
$\omega_0^{H \rightarrow P}/2\pi$ [kHz]	98	108
$\Gamma_{H \rightarrow P}$ (T=1 mK) [Hz]	6.13×10^1	3.39×10^{-13}
$\Gamma_{H \rightarrow P}$ (T=5 mK) [Hz]	1.08×10^5	4.05×10^2

Table 3.1: The parameters relevant to equation 3.1.2 and the rates of transition associated with the minimum energy paths for M2=9 and M2=10. The energy barrier is given by E_b , the average frequency of the many-body calculation is given by ν^* , and the rate of transition across the potential boundary according to the many-body rate calculation is given by $\Gamma(T)$. The values of the curvature around the minima on the MEP are given by $\omega_0/2\pi$, which would be used for a one-dimensional Transition State Theory rate calculation.

a system with zero kinetic energy would take between local minima, so the path can take sharp and sudden turns that particles with momentum would be unable to make. We still use these paths for classical rate calculations, however, because they present the lower bound of the energy barrier.

From equation 3.1.2, we are able to calculate approximate rates at which the system would transition over the energy barrier for given temperatures. This data is summarized in table 3.1.4. In addition to the parameters necessary to calculate $\Gamma(T)$ for a many-body system, we have included values for $\omega_0/2\pi$ for each minimum energy path. This is a measure of the curvature in the potential wells along the MEP, and it may be used in place of ν^* in a one-dimensional TST analysis of the potential surface along the MEP. It is worth noting that $\omega_0/2\pi$ is considerably smaller than ν^* .

The TST rates, $\Gamma(T)$, exhibit a significant temperature dependence for temperatures an order of magnitude smaller than the energy barrier. This results in a large discrepancy between the rates of transition in different directions. We do not know what are expected values for the rates of transition

in different directions because equation 3.1.2 assumes all transitions to be moving in one direction (treating the transition from $H \rightarrow P$, for example, as if it were a transition from H over a potential barrier and into an infinite potential well), whereas the actual system transitions back and forth between states. By comparing $\Gamma_{H \rightarrow P}/\Gamma_{P \rightarrow H}$ to data showing t_P/t_H , where t_P is the total amount of time spent in the pentagonal state, we can approximate the temperature of the system.

It is worth noting that this classical analysis only takes thermally-activated transitions into account. Another collaborator on this project, Dr. Alex Levine, is working on a numerical model of “noise” in the system. The noise that he is modeling consists of fluctuations in the amplitude of the voltages in the trap that “kick” the ions around in a way that is described by the Fokker-Planck equation (i.e. that is akin to Brownian motion). This analysis also takes into account only classical mechanics, but it is much more accurate than our own because it follows Newton’s laws of motion throughout the transition, and therefore can account for particle momentum at various points along the path.

Quantum Tunneling

For a purely classical, thermally-activated transition, the minimum energy path is the ideal transition pathway. This is because the transition relies on energetic excitations to overcome the potential energy barrier, and the probability of transitioning along a path does not decrease as the path length increases. This is not the case for quantum tunneling.

Quantum tunneling occurs when a wavefunction encounters a region from which it is classically forbidden (i.e. the potential energy in that region is greater than the energy of the wavefunction). Consider, as an example, the solution to the time-independent Schrodinger equation for a free particle of energy E . The TISE is given by

$$[-\frac{\hbar^2}{2m} \frac{d^2}{dx^2} + V(x)]\psi(x) = E\psi(x). \quad (3.12)$$

Let’s further say that the potential energy, $V(x)$, is zero everywhere except for the region $-a \leq x \leq a$, within which it is equal to $V_0 > E$. The free particle, therefore, is classically forbidden within that region. By shifting around equation 3.12, we find

$$\frac{\hbar^2}{2m} \frac{d^2}{dx^2} \psi(x) = (V(x) - E)\psi(x). \quad (3.13)$$

In the regions in which $V(x) = 0$, the right side of equation 3.13 is negative and $\psi(x)$ will be a complex exponential function. This is simply the solution to the TISE for a classically-allowed free particle, as the spatial probability distribution, $|\psi(x)|^2$, is uniform, meaning that the probability of finding the particle in any location is equal. In the classically-forbidden region, however, the right side of equation 3.13 is positive, meaning that the solution for $\psi(x)$ is a real exponential function: $\psi(x) = B_+ \exp(\kappa x) + B_- \exp(-\kappa x)$. Noting that, in principle, the width of the classically-forbidden region can be as long as we want it to be, and that the probability distribution of the free particle should not be able to increase infinitely, the correct solution within the classically-forbidden region must be $\psi(x) = B_- \exp(-\kappa x)$. The quantum mechanical solution to a free particle in a classically-forbidden region, then, does not exclude the possibility that the particle traverses that region. Rather, the wavefunction may penetrate the barrier, but the probability that it does so decays exponentially with the width of the barrier.

In order to get a sense as to whether a detailed quantum mechanical analysis of the Coulomb crystal system would be worthwhile, we performed the Wentzel-Kramers-Brillouin (WKB) approximation. This is an approximate plane-wave solution to the Schrodinger equation for a potential, $U(x)$, that varies slowly in space. In this approximation, the wavefunction may be written as $\psi(x) = A \exp(i\phi(x))$, where $\phi(x) = xk(x)$ [29]. We can define $k(x) = \sqrt{\frac{2m}{\hbar^2}(E - U(x))}$ for $E > U(x)$ and $k(x) = -i\sqrt{\frac{2m}{\hbar^2}(U(x) - E)}$ for $E < U(x)$. Under these conditions, the solution to equation 3.12 is

$$i \frac{d^2\phi}{dx^2} - \left(\frac{d\phi}{dx} \right)^2 + (k(x))^2 = 0. \quad (3.14)$$

If we assume $k(x)$ to be slowly-varying, which is an extension of the fact that $U(x)$ is slowly-varying, then we can assume that $\phi(x)$ is slowly-varying as well. This means that $\frac{d^2\phi}{dx^2} \approx 0$, so $(\frac{d\phi}{dx})^2 = (k(x))^2$ and $\phi(x) = \pm \int k(x) dx + C_0$. This leaves us with our zeroth order WKB approximation of $\psi(x)$ in a classically-forbidden region:

$$\psi(x) = \exp\left(-\int \sqrt{\frac{2m(U(x) - E)}{\hbar^2}} dx + C_0\right). \quad (3.15)$$

The probability of tunneling through a classically-forbidden boundary that spans from $x = a$ to $x = b$ is therefore

$$T = \exp\left(-2 \int \sqrt{\frac{2m(U(x) - E)}{\hbar^2}} dx\right). \quad (3.16)$$

We applied this zeroth-order, one-dimensional approximation to each of the calculated MEPs and found probabilities of transitioning on the order of $\exp(-10^5)$. We also applied this approximation to the paths used to approximate the energy barrier, and we found that they all gave higher probabilities for quantum tunneling than the MEP. The reason for this is that the probability of tunneling decays exponentially with distance, and although the MEP is the lowest-energy transition pathway, it is also the longest (among those listed here). The probability of tunneling along any of the pathways presented in this thesis, however, is not greater than $\exp(-10^4)$, so we can conclude that the Coulomb crystal system is not tunneling between states.

3.2 Data Analysis

3.2.1 Markov Chain

A Markov process is a stochastic (random) process that satisfies the property $p(x_n|x_{n-1}, x_{n-2}, \dots) = p(x_n|x_{n-1})$ [31]. This property, also called the Markov property, means simply that the probability of any future state of the system is dependent only on the state that immediately precedes it. The simplest model of a Markov process is the Markov Chain, wherein there exists a countable set of potential states of a system and every state has a specified probability of transitioning to any other state. In our case, there are only two possible states (a closed ring state and an open ring state), and there are only two transition probabilities associated with each state: the probability of transitioning to the other state after a given time step, and the probability of remaining in the same state after a given time step.

The probability of a particular sequence of states, $[x_0, x_1, x_2, \dots, x_n]$, is given by $P(x_0) \prod_{i=1}^n P(x_i|x_{i-1})$, the product of the transition probabilities that describe the given sequence. We assume the transition probabilities to be constant in time, so the probability of a given sequence of states does not depend on the order in which transitions occur. This allows us to determine the transition probabilities very easily from a set of data. Take, for instance,

a two state system in which the possible states are A and B . In a data set in which there are n data points, there are $n - 1$ transitions between data points (e.g. $x_1 \rightarrow x_2$, $x_2 \rightarrow x_3$, etc.). Each data point indicates whether the system is in state A or state B at a given time. The probability of transitioning from state A to state B , then, is simply given by dividing the number of transitions from $A \rightarrow B$ divided by the number of transitions in which the system began in state A . This latter term is the sum of the number of transitions from $A \rightarrow B$ and the number of transitions from $A \rightarrow A$. This can be summarized by writing the transition matrix as

$$\begin{pmatrix} p_{A \rightarrow A} & p_{A \rightarrow B} \\ p_{B \rightarrow A} & p_{B \rightarrow B} \end{pmatrix} = \begin{pmatrix} \frac{n_{A \rightarrow A}}{n_{A \rightarrow A} + n_{A \rightarrow B}} & \frac{n_{A \rightarrow B}}{n_{A \rightarrow A} + n_{A \rightarrow B}} \\ \frac{n_{B \rightarrow A}}{n_{B \rightarrow A} + n_{B \rightarrow B}} & \frac{n_{B \rightarrow B}}{n_{B \rightarrow A} + n_{B \rightarrow B}} \end{pmatrix}, \quad (3.17)$$

where $p_{A \rightarrow B}$ is the probability of transitioning from state A to state B , and $n_{A \rightarrow B}$ is the number of transitions from A to B in a given set of data.

The Markov chain, however, is a very simplistic representation of the Coulomb crystal system. The actual system, of course, does not have just two possible states. That said, we accept this to be a reasonable simplification because experimental evidence from the Campbell group indicates that the system spends the vast majority of its time in the two potential wells, and that it transitions between wells on a timescale much shorter than the amount of time it spends in either. This justifies treating the transition as a discontinuous transition between two states. The second shortcoming of the Markov chain, though, is that it operates on a discrete timescale, whereas the actual Coulomb crystal system operates on a continuous timescale. The fact that the Campbell group measured the system at specific, regular times discretizes the data such that a Markov chain analysis is possible, but the transition probabilities that result from such an analysis are dependent on the time in between measurements.

3.2.2 Continuous Time Markov Chain

A more realistic representation of the Coulomb crystal system is a continuous time Markov chain (CTMC). Like the discrete time Markov chain, the CTMC operates on a countable state space. The difference, however, is that transitions can occur at any time in a CTMC rather than at only discrete points in time. We can define the amount of time that the system spends in a given state, i , as a random variable called the holding time, H_i [30]. After

the holding time is complete, the system will transition from state i to state j with a probability p_{ij} . For two-state systems, this probability is always equal to 1 because a state cannot transition from state i into state i in a CTMC; rather, it is “held” in state i for the extent of the holding time, after which it must (by definition) transition into the other state. The Markov property for a CTMC may be summarized by saying that the probability that the system is in state j at time $s + t$ given that it was in the state i at time t , for all times $t > 0$ and $s > 0$, is independent of the state of the system before t .

Note that the holding time is a random variable, so we are looking to solve for properties of the distribution of holding times rather than exact values of the holding time. As the distribution of holding times must be memoryless (as is required by the Markov property) and holding times can take the value of any non-negative real number, holding times must be distributed according to the exponential distribution. An exponential distribution is defined by a characteristic rate, λ_i , such that $P(H_i \leq t) = 1 - \exp(-\lambda_i t)$ for $t > 0$. The rate associated with a given state is constant in time, which is why I have labelled it as λ_i for the state i . The expected value of an exponential distribution is $E(H_i) = 1/\lambda_i$.

While the data we have from the Campbell group represents measurements made at discrete times, we know that transitions between states of the Coulomb crystal can occur at any time. We can therefore use the data we have to approximate the average holding time in each state, from which we can determine the rate constant of the exponential distribution.

3.2.3 Results

The data sent to us by the Campbell group is presented in figure 3.6. Time is reported on the x-axes and light intensity is reported on the y-axes. The Campbell group scatters light off the crystal and collects the scattered photons in a photomultiplier tube. The state of higher intensity corresponds to the hexagonal state and the state of lower intensity corresponds to the pentagonal state. The intensity is given in units of kilo-counts (of photons) per second. The Campbell group also reports values for “M2,” which is a monotonic function of the strength of the symmetry-breaking potential, ϕ_{aniso} . We do not know the precise relationship between M2 and ϕ_{aniso} , however. Measurements of the M2=9 system were taken every 0.1 sec for a total of 304 sec, while the measurements of the M2=10 and M2=11 systems were taken every 0.05 sec for a total of 654 sec and 270 sec, respectively.

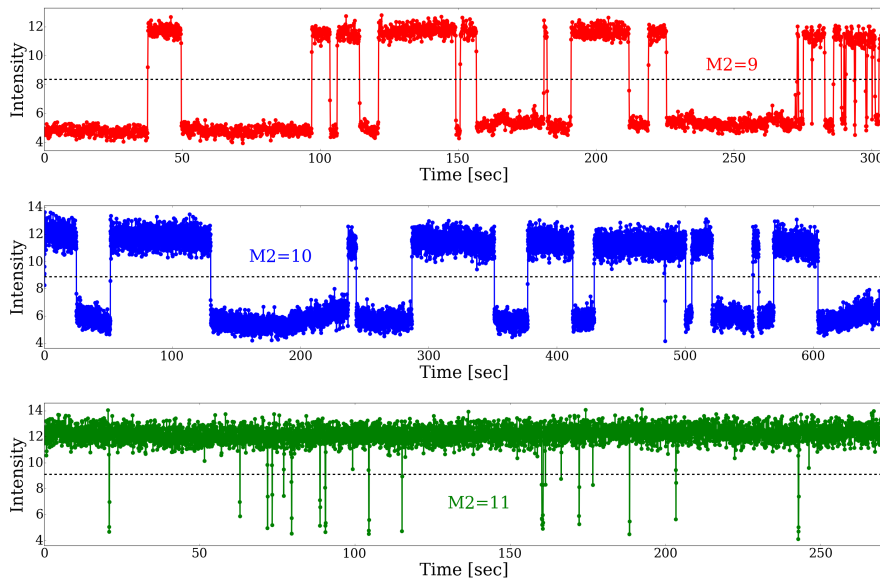


Figure 3.6: Measurements taken by the Campbell group of the intensity of scattered light (units of kilo-counts per second) over time for three different values of M_2 (monotonically related to ϕ_{aniso}). The higher intensity state corresponds to the hexagonal state of the Coulomb crystal, and the lower corresponds to the pentagonal state. The black dotted line is the average value of the intensity between the two states, and is used to divide the data into a two-state subspace such that a Markov chain analysis can be applied.

In order to translate this data into two-state space, I determined an average value between extrema of the intensity for each plot. These are marked as black dotted lines on figure 3.6. The average values of the intensity for M2=9, M2=10, and M2=11 are 8.37, 8.88, and 9.11 kilo-counts per second, respectively. All values of the intensity that were greater than or equal to this average value were considered to be in the hexagonal state, and all values less than that value were considered to be in the pentagonal state. The transition matrices below describe the data from the discrete time Markov chain analysis:

$$T_{M2=9} = \begin{pmatrix} p_{H \rightarrow H} = 0.985 & p_{H \rightarrow P} = 0.015 \\ p_{P \rightarrow H} = 0.009 & p_{P \rightarrow P} = 0.991 \end{pmatrix}$$

$$T_{M2=10} = \begin{pmatrix} 0.998 & 0.002 \\ 0.002 & 0.998 \end{pmatrix}$$

$$T_{M2=11} = \begin{pmatrix} 0.997 & 0.003 \\ 0.367 & 0.633 \end{pmatrix}$$

We can gain insight into the shape of the potential surfaces by comparing the relative sizes of $p_{H \rightarrow P}$ and $p_{P \rightarrow H}$, which we would expect to be related to the relative sizes of the rates of transition in a classical, thermally-activated system. The values of $p_{H \rightarrow P}/p_{P \rightarrow H}$ for M2=9, M2=10, and M2=11 are 1.627, 1.047, and 0.009, respectively. This indicates that the rate of transition from the hexagonal to the pentagonal state is slightly favored for M2=9, whereas the rates of transition are roughly equivalent for M2=10. As expected, the M2=11 system transitions much more often from the pentagonal state to the hexagonal state than vice versa.

If we believe this to be a thermally-activated transition, a larger rate of transition in one direction should correspond with a lower energy barrier (i.e. an initial state with a higher energy) or a larger curvature in the initial potential well. It is therefore worth noting a difference between my guess at the M2=10 parameters and the results of the discrete time Markov chain analysis. As shown in figure 3.5, the energy barrier in the $H \rightarrow P$ transition is much larger than that of the $P \rightarrow H$ transition, which meant that the relative rates of transition differed by multiple orders of magnitude. The data from the Campbell group, however, shows that the probabilities of transitioning in either direction for M2=10 are nearly identical. This is likely due to the shortcomings of my method for guessing corresponding parameters,

	M2=9	M2=10	M2=11
Average Holding Time Pent [sec]	10.583	26.810	0.086
Average Holding Time Hex [sec]	6.388	30.418	13.312
λ_P [Hz]	0.094	0.037	11.607
λ_H [Hz]	0.156	0.033	0.075

Table 3.2: The average holding time in the pentagonal and hexagonal states for each value of M2. The characteristic frequencies, λ_i , are the inverse of the average holding times.

as was discussed in the previous section. Another possible reason for this discrepancy could be the path that the system takes to transition between states: if the system takes a path with a significantly higher energy barrier than the one displayed in figure 3.5, the difference between the energies of the local minima will be smaller compared to the difference between the energy of either minimum and that of the saddle point. This means that the rates of transition in both directions will decrease and that $p_{H \rightarrow P}/p_{P \rightarrow H}$ should approach 1. The Campbell group has been unable to take images of the trapped-ion system during a transition, though, so we do not have enough information to say whether or not this could be the case.

The discrete time Markov chain analysis, however, does not account for the actual amount of time that the system spends in either local minimum before transitioning. This is notable because, as mentioned earlier, the length of time between measurements for the M2=9 data is twice that of the M2=10 data. While this discrepancy should not affect the relative probabilities of transitioning, it is an important point of comparison between the different systems. By measuring the average amount of time that the system spends in one of the states before transitioning, we can approximate the expected value of the holding time and the characteristic rate of the distribution. These values are summarized for each data set in table 3.2.3.

The relative sizes of the characteristic frequencies in each system align with our expectations based on the transition matrices from the discrete time Markov chain analysis. The relative lengths of the holding times between different sets of parameters is notable, however, as the M2=10 system displays significantly longer holding times in both directions than either of the other two states. The rapid transitions during the last 50 sec of the M2=9 mea-

surements certainly exaggerate this difference, but it is evident nonetheless upon inspection of the timescale in figure 3.6. This is unexpected because our computational analysis of the MEP did not indicate any significant increase in the overall energy barrier or decrease in curvature in the potential wells. The result may therefore indicate that the system transitions using a path other than the MEP.

3.3 Conclusions

Computational models of the potential surface in the oblate Paul trap have allowed us to examine the energy barrier between the two stable conformations of the Coulomb crystal. While we are unable to determine the precise path that the system takes between states, the paths presented in section one of this chapter give upper and lower limits for the energy barrier between states. These can be used to determine the rate of thermally-activated transitions from one well to the other. When we are given the parameters that correspond with measurements of the Coulomb crystal transition, we hope to use this analysis as an effective thermometer for the system.

The use of discrete and continuous time Markov chain analyses also allows us to gain insight into the height of the potential barrier and the curvature at the bottom of the potential wells along the actual transition pathway. In conjunction with the work of Dr. Levine on models for noise in the trapped ion system, we hope to be able to characterize the path of and the energetic contributions to this transition.

Chapter 4

Final Remarks

4.1 Rough Timeline

The work presented in this thesis has been completed over a larger time span than the usual two semesters, so I would like to clarify at what times the different aspects of this research were completed.

Chronologically, the first project I completed was that which is presented in chapter two. I began work on it with Professor Freericks during January 2015, the second semester of my freshman year. I spent the extent of that semester familiarizing myself with spin dynamics and the XY and transverse-field Ising models. Over the following Summer, I taught myself how to code in Python. This effort continued into my sophomore year, during which I wrote all of the code necessary to evolve the Hamiltonians in Python and began to frame the problem we were investigating. The following Summer (2016), I worked with the Awschalom group at the University of Chicago and did not make significant headway on this project. I then studied abroad during the Fall 2016 semester at the University of Bologna, where I focused on staying acquainted with the project rather than making further progress. The Spring 2017 semester was spent re-familiarizing myself with the programs I had written and beginning to narrow down the material that would be covered in a paper. I stayed on campus to continue working with Professor Freericks over the Summer of 2017, and it was during this time period that I completed the final calculations and began making figures and writing the paper. The paper-writing process continued into the first two and a half months of the Fall 2017 semester, after which we spent about two weeks working on referee

reports. The paper was submitted in November of 2017 and was accepted for publication in January of 2018.

Work on the second project began in earnest only after the submission of the paper. The third chapter of this thesis, therefore, is the result of about a semester of work.

4.2 Acknowledgments

First and foremost, I would like to thank my senior thesis advisor and research supervisor for seven of my eight semesters at Georgetown, Dr. James Freericks. He taught me a tremendous amount about his research, about the methods of conducting research, about scientific writing, and about the field of physics in general over the course of my undergraduate career. I am also grateful that he allowed both of these projects to be my own work, at least to the extent possible at an undergraduate level.

I would also like to acknowledge the work put forth by collaborators towards this research project: Dr. Chris Monroe and his group at the University of Maryland; Dr. Wes Campbell and his group at UCLA, including Anthony Ransford; Dr. Alex Levine at UCLA; and Harry Han, Georgetown Class of 2017, who worked on computational modeling of the Campbell group's Coulomb crystal for his senior thesis as well.

I would also like to thank my second reader and mentor for all four years, Dr. Joseph Serene. He taught my first Physics course at Georgetown and has since been a constant supporter of my endeavors and a close advisor on virtually all matters. I cannot quantify the amount I have learned from him and the extent to which he has shaped my time at Georgetown.

To that end, I want to thank the Georgetown Physics department in general. I have been fortunate to have been surrounded by so many professors who took genuine interest in my activities and my success.

Finally, I would like to thank my parents, my friends, and my girlfriend for supporting me when I was overworked or discouraged. Thank you.

Bibliography

- [1] R. Feynman, *The Character of Physical Law*. The M.I.T. Press, 1965.
- [2] R. Feynman, Int. J. Theor. Phys. **21**, 6/7 (1982).
- [3] B. Yoshimura, M. Stork, D. Dadic, W. C. Campbell, and J. K. Freericks, EPJ Quantum Technology **2**, 2 (2015).
- [4] C. R. Senko, “Dynamics and Excited States of Quantum Many-Body Spin Chains with Trapped Ions”, PhD thesis, University of Maryland, College Park, 2014.
- [5] R. Feynman, Int. J. Theor. Phys. **9**, 1 (1966).
- [6] D. Jurafsky and J. H. Martin, *Speech and Language Processing*. Prentice Hall, 2008.
- [7] K. Kim, M.-S. Chang, S. Korenblit, R. Islam, E. E. Edwards, J. K. Freericks, G.-D. Lin, L.-M. Duan, and C. Monroe, Nature **465**, 590 (2010).
- [8] R. Islam, E. E. Edwards, K. Kim, S. Korenblit, C. Noh, H. Carmichael, G.-D. Lin, L.-M. Duan, C.-C. Joseph Wang, J. K. Freericks, C. Monroe, Nature Commun. **2**, 377 (2011).
- [9] Joseph W. Britton, Brian C. Sawyer, Adam Keith, C.-C. Joseph Wang, J. K. Freericks, Hermann Uys, Michael J. Biercuk, John. J. Bollinger, Nature **484**, 489 (2012).
- [10] R. Islam, C. Senko, W. C. Campbell, S. Korenblit, J. Smith, A. Lee, E. E. Edwards, C.-C. J. Wang, J. K. Freericks, and C. Monroe, Science **340**, 583 (2013).

- [11] C. Senko, J. Smith, P. Richerme, A. Lee, W. C. Campbell, and C. Monroe, Science **345**, 430 (2014).
- [12] P. Richerme, Z.-X. Gong, A. Lee, C. Senko, J. Smith, M. Foss-Feig, S. Michalakis, A. V. Gorshkov, and C. Monroe, Nature **511**, 198 (2014).
- [13] P. Jurcevic, B. P. Lanyon, P. Hauke, C. Hempel, P. Zoller, R. Blatt and C. F. Roos, Nature **511**, 202 (2014).
- [14] Martin G  rttner, Justin G. Bohnet, Arghavan Safavi-Naini, Michael L. Wall, John J. Bollinger and Ana Maria Rey, Nature Physics **13**, 781 (2017).
- [15] J. Zhang, P.W. Hess, A. Kyprianidis, P. Becker, A. Lee, J. Smith, G. Pagano, I.-D. Potirniche, A.C. Potter, A. Vishwanath, N.Y. Yao, C. Monroe, Nature **543**, 217 (2017).
- [16] J. Smith, A. Lee, P. Richerme, B. Neyenhuis, P. W. Hess, P. Hauke, M. Heyl, D. A. Huse, and C. Monroe, Nature Physics **12**, 907 (2016).
- [17] J. Zhang, G. Pagano, P. W. Hess, A. Kyprianidis, P. Becker, H. B. Kaplan, A. V. Gorshkov, Z.-X. Gong, and C. Monroe, *preprint arXiv 1708.01044* (2017).
- [18] E. Lieb and D. Robinson, Commun. Math. Phys. **28**, 251 (1972).
- [19] S.-L. Zhu, C. Monroe, and L.-M. Duan, Phys. Rev. Lett. **97**, 050505 (2006).
- [20] D. F. V. James, Appl. Phys. B **66**, 181 (1998).
- [21] C. Marquet, F. Schmidt-Kaler, and D. F. V. James, Appl. Phys. B **76**, 199 (2003).
- [22]] M. Knap, A. Kantian, T. Giamarchi, I. Bloch, M. D. Lukin, and E. Demler, Phys. Rev. Lett. **111**, 147205 (2013).
- [23] M. Serbyn, M. Knap, S. Gopalakrishnan, Z. Papi , N.  Y. Yao, C. Laumann, D. Abanin, M. Lukin, and E. Demler, Phys. Rev. Lett. **113**, 147204 (2014).
- [24] Bryce T. Yoshimura and J. K. Freericks. Phys. Rev. A **93**, 052314 (2016).

- [25] M. H. Lim, B. T. Yoshimura, and J. K. Freericks, New J. Phys. **18**, 043026 (2016).
- [26] P. Hanggi, J. Stat Phys. **42**, 105 (1986).
- [27] G. Henkelman, G. Johannesson, and H. Jonsson, *Theoretical Methods in Condensed Phase Chemistry*. Springer Netherlands, 2002.
- [28] D. Sheppard, R. Terrell, and G. Henkelman, J. Chem. Phys. **128** 134106 (2008).
- [29] A. Doolittle, “Lecture 8: WKB Approximation, Variational Methods and the Harmonic Oscillator,” Georgia Tech.
- [30] K. Sigman, “IEOR 6711: Continuous-Time Markov Chains,” Columbia University, 2009.
- [31] P. Glynn, “Section 2: Discrete Time Markov Chains,” Stanford University, MS&E 321, 2013.